Physics of Fluids ARTICLE scitation.org/journal/phf

Role of Atwood number on flow morphology of a planar shock-accelerated square bubble: A numerical study

Cite as: Phys. Fluids 32, 126112 (2020); doi: 10.1063/5.0031698
Submitted: 5 October 2020 • Accepted: 29 November 2020 •
Published Online: 15 December 2020

View Online Export Citation CrossMark

Satyvir Singh[a)]

AFFILIATIONS

School of Physical and Mathematical Sciences, Nanyang Technological University, 21 Nanyang Link, Singapore 637371

Note: This paper is part of the Special Topic, Advances in Micro/Nano Fluid Flows: In Memory of Prof. Jason Reese.
[a)]**Author to whom correspondence should be addressed:** satyvir.singh@ntu.edu.sg

ABSTRACT

The Atwood number plays a critical role in describing the physics of fluids behind the hydrodynamic instabilities in gas dynamics. In order to investigate the impacts of the Atwood number (At), the evolution of a shock-accelerated square bubble containing either SF_6, Kr, Ar, Ne, or He and surrounded by N_2 is investigated numerically. For this purpose, the unsteady compressible Navier–Stokes–Fourier equations are solved using an explicit modal discontinuous Galerkin method. For validation, the numerical results are compared with available experimental results and are found to be in good agreement. The results demonstrate that the Atwood number has a significant influence on flow morphology with wave patterns, vortex creation, vorticity generation, and bubble deformation. For At > 0, the speed of the shock wave traveling along with the bubble inner surface is often less than that of the incident shock wave and greater than that of the transmitted shock wave. Moreover, vortex pairs from the upstream and downstream corners are generated, and the former vortex pair ultimately dominates the flow morphology. For At ≈ 0, the incident and transmitted shock waves move at the same speeds, whereas for At < 0, the transmitted shock wave travels faster than the incident shock wave. Moreover, only one vortex pair at the upstream corners is generated, which dominates the flow morphology. Furthermore, a detailed study of Atwood number impacts is investigated through the vorticity generation at interfaces. A quantitative analysis based on the shock trajectories, the interface features, and the integral diagnostics is also studied in detail to investigate the impacts of the Atwood number on the flow structure. Finally, a comparative study of the flow physics between the shock-accelerated square and cylindrical bubbles is conducted to examine their natural differences.

Published under license by AIP Publishing. https://doi.org/10.1063/5.0031698

I. INTRODUCTION

The Richtmyer–Meshkov (RM) instability[1,2] is one of the well-known fluid interface instabilities leading to a turbulent mixing zone in nature. The RM instability is a physical phenomenon that arises when a planar shock wave impulsively accelerates an arbitrarily perturbed interface separating two fluids of different densities. Owing to the misalignment between the pressure gradient of the shock wave and the local density gradient across the arbitrarily disrupted interface, this instability is triggered by the baroclinic vorticity generation at the interface. The RM instability is ubiquitous in many natural and engineering applications, including inertial confinement fusion,[3] supernova explosions,[4] medical shock wave lithotripsy,[5] scramjet combustion process,[6,7] stellar evolution models in astrophysics,[8] and many more as surveyed in the review of Brouillette.[9]

Numerous experimental, theoretical, and computational studies have been performed and published in the past to explain the physical phenomenon of the RM instability. Planar shock-accelerated bubbles, referred to as shock–bubble interaction, are widely considered for studying the RM instability. At first time, Markstein[10] and Rudinger and Somers[11] investigated the shock–bubble interaction experimentally to describe a complex turbulent flow field phenomenon with long-living vortex rings. Haas and Sturtevant[12] investigated experimentally the interaction of a planar, weak shock wave with a single gas bubble containing either helium, refrigerant, or fluorocarbon by using a shadowgraphy technique and described the flow morphology phenomenon for both

Published under license by AIP Publishing

divergent and convergent conditions. Subsequently, the interaction between a weak shock wave and cylindrical light/heavy gas bubbles was experimentally investigated using a planar laser induced fluorescence technique by Jacobs,[13,14] and high quality flow morphology visualization was observed. Layes *et al.*[15–17] investigated experimentally the interaction between a plane shock wave and a bubble containing different gases such as helium, nitrogen, and krypton using a high-speed camera shadowgraph diagnostic. The experimental results obtained could be used to test other numerical and theoretical studies. Meanwhile, Ranjan *et al.*[18] investigated the physics for shock-spherical bubble interaction in divergent shock-refraction geometry using shock tube experiments.

Generally, the flow morphology of the shock–bubble interaction essentially depends on a dimensionless parameter called the Atwood number defined as

$$\mathrm{At} = \frac{\rho_b - \rho_g}{\rho_b + \rho_g}, \quad \text{with} \quad -1 \le \mathrm{At} \le 1. \tag{1}$$

Here, ρ_b and ρ_g are the densities of the bubble gas and its surrounding gas, respectively. To demonstrate the impact of the Atwood number on the shock–bubble interactions, two different values of the Atwood number (At = 0.17 and 0.68) were tested experimentally by Haehn *et al.*[19] The results revealed a secondary vortex ring for the low Atwood number immediately after a reshock. Numerous experimental sets of He and SF_6 bubbles surrounded by air with high-speed schlieren photography were performed by Si *et al.*[20]

Besides the experimental works described above, various studies on the shock-accelerated bubble were also carried out numerically. Quirk and Karni[21] performed a detailed numerical investigation on the flow morphology of the shock-accelerated cylindrical gas bubble based on Haas and Sturtevant's experimental results.[12] Zabusky and Zeng[22] investigated numerically the planar shocks interacting with a Refrigerant-12 axisymmetric spherical bubble and showed the evolving upstream and downstream complex wave patterns and emphasized the appearance of vortex rings. Bagabir and Drikakis[23] subsequently numerically analyzed the incident shock Mach number effects on the shock-accelerated cylindrical bubble, revealing additional gas dynamics with the rising shock Mach numbers. Niederhaus *et al.*[24] performed an extensive numerical study of the three-dimensional shock-accelerated spherical bubble to investigate the flow morphology and time-dependent integral properties, including the impacts of the Atwood number ($-0.8 < \mathrm{At} < 0.7$) and the shock strengths ($1.1 < M_s < 5.0$). Later, Zhai *et al.*[25] studied numerically the shock-accelerated spherical bubble containing various gases (SF_6 and He) using the VAS2D code and investigated the flow morphology, including the evolution of interfaces and the development of wave patterns. Thereafter, Zou *et al.*[26] explored numerically the evolution of heavy bubbles with different gases (SF_6, R22, R12, and Kr) in a shock accelerated flow, and the influences of the different gases on the shock wave focusing and jet formation were investigated. Recently, Zhu *et al.*[27,28] studied numerically the shock-accelerated cylindrical bubble to investigate the deformation and instability of light and heavy bubbles, the formation and evolution of vortex rings, shock wave patterns, the shock focusing processes, and jet formation mechanisms.

Interestingly, most of the earlier experimental, theoretical, and computational studies have investigated the interaction between an incident shock wave and bubbles of different shapes, including cylindrical, elliptical, or spherical. So far, there are a few studies available on the shock-accelerated gas bubbles having polygonal interfaces that provide good conditions for shock refraction physical phenomena. This type of research has various practical applications, for example, a helium-filled balloon over a volcanic mountain for providing an early warning of a developing eruption. When such an eruption happens, there is an interaction with the produced blast wave that propagates in the air with a bubble containing a different gas. Zhai *et al.*[30] investigated experimentally and numerically the interaction of a planar shock wave with polygonal N_2 interfaces (square, triangle, and diamond) surrounded by SF_6. Emphasis was placed on the investigation of the wave pattern of the shock refraction at the slow/fast interface and the effects of the interface shape on the interface morphology. Later, this study was extended to explore the shock refraction phenomenon at a fast/slow interface and the effect of the initial interface shape on the RMI through dealing with the interaction of a planar shock wave with six different SF_6 polygons (a square, two rectangles, two triangles, and a diamond) surrounded by air.[31] Igra and Igra[32] studied numerically the interaction between a planar shock wave and square and triangular bubbles containing either SF_6, He, Ar, or CO_2. Subsequently, this work was further extended for the interaction between a planar shock wave propagating in air and a polygonal bubble (composed of two triangles) containing two different gases.[33] Recently, a series of heavy gas inhomogeneities with very simple geometries (square, rectangle, circle, and triangle) were numerically reproduced to trace the source of the jet formation by Fan *et al.*[34]

Encouraged by these developments, the shock-accelerated square bubble is again revisited in this study, and the impacts of the Atwood number at several values (At = 0.667, 0.466, 0.074, −0.218, and −0.773, corresponding to SF_6, Kr, Ar, Ne, and He, respectively) on the flow morphology of the square bubble surrounded by N_2 are comprehensively investigated numerically. The reason behind for the selection of these Atwood numbers is that the related gases have been widely adopted in the above-mentioned research works for the Richtmyer–Meshkov instability study. Emphasis is placed on the flow morphology visualization, wave patterns, vorticity generation, and their quantitative analysis based on the shock-trajectories, interface features, and integral diagnostics. For a comparative analysis of flow physics between the shock-accelerated square and cylindrical bubbles in depth, a numerical investigation is also performed. Furthermore, the present work can be seen as a supplement to the RM instability research to examine the Atwood number effects on the dynamics of a shock-accelerated square bubble (such as shock refraction phenomenon, shock-focusing, and jet formation).

Toward this goal, this paper is structured as follows: In Sec. II, the computational model including the problem setup and numerical method are presented. In Sec. III, the grid refinement analysis and the validation of numerical method are studied. In Sec. IV, the computational results for the Atwood number impacts on a shock-accelerated square bubble are discussed in details. First, the general features of the flow morphology in the shock-accelerated square bubble are presented. After then, numerical results obtained with a high grid resolution for flow evolution visualization at different Atwood numbers are presented. Furthermore, the influences of the

Published under license by AIP Publishing

Atwood number on the vorticity generation and their quantitative analysis are also investigated. Consequently, a comparative study of the flow physics between the shock-accelerated square and cylindrical bubbles is conducted to investigate their natural differences. Finally, conclusions remarks with further development in line of the present study are given in Sec. V.

II. PROBLEM SETUP AND COMPUTATIONAL MODEL

A. Problem setup

Figure 1 illustrates a schematic diagram of the flow model used to simulate a planar incident shock wave interacting with a square bubble surrounded with ambient gas. The computational domain is a rectangular two-dimensional space with length $L = 200$ mm and width $W = 140$ mm in the directions of x and y, respectively. In this study, a moving planar incident shock wave and stationary square bubble are considered. The planar shock wave with the Mach number $M_s = 1.21$ propagates from left to right in the x–direction. The initial position of the shock wave is at $x = 20$ mm from the left-hand side of the computational domain. The edge length of the square bubble is set to $a = 56.6$ mm based on the experimental study conducted by Luo *et al.*[31] The ambient gas is nitorgen (N_2) with initial pressure $P = 101\,325$ Pa and room temperature $T = 298$ K around the bubble, while a light gas (He or Ne) or a heavy gas (SF_6, Kr, or Ar) is used as the testing gas within the inhomogeneity. The left boundary is set to be inflow, while the upper, bottom, and right boundaries are set to be outflow boundaries.

B. Governing equations

The shock-accelerated inhomogeneous flow problems are basically solved by simulating the compressible multi-species flow model with a gas mixture.[35,36] Interestingly, it has been found in the previous research works of Picone and Boris,[37] Samtaney and Zabusky,[38] Quirk and Karni,[21] and Bagabir and Drikakis[23] that the different values of specific heat capacities γ values for each gas do not affect the details of the vorticity generation qualitatively, particularly the creation of large-scale structures. According to Quirk and Karni,[21] for the problem of shock–bubble interaction, "...the errors introduced by the single-gas model assumption are not catastrophic and to some extent may be tolerated," but such errors cannot be tolerated in other applications, for example, air–fuel mixing in a supersonic combustion system, where temperature changes will substantially affect the mixing. Based on the above-mentioned discussion, the present shock-accelerated square bubble problem is modeled through the unsteady compressible laminar flow, which assumes a single-component perfect gas with specific heat ratio γ.

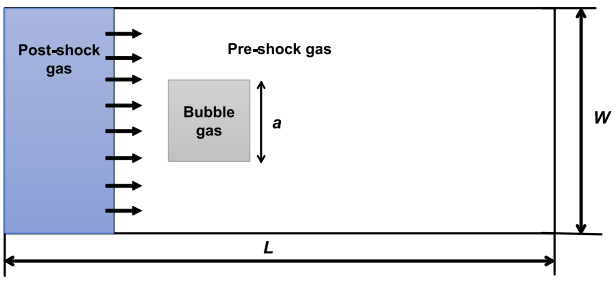

FIG. 1. Problem setup: schematic diagram of initial flow field and computational domain.

Here, we consider the two-dimensional compressible Navier–Stokes–Fourier (NSF) equations for the laminar flow model. The unsteady compressible NSF equations[39,40] are written in conservation form,

$$\frac{\partial \mathbf{U}}{\partial t} + \frac{\partial \mathbf{F}^{inv}}{\partial x} + \frac{\partial \mathbf{G}^{inv}}{\partial y} + \frac{\partial \mathbf{F}^{vis}}{\partial x} + \frac{\partial \mathbf{G}^{vis}}{\partial y} = 0, \tag{2}$$

where

$$\mathbf{U} = \begin{bmatrix} \rho \\ \rho u \\ \rho v \\ \rho E \end{bmatrix}, \quad \mathbf{F}^{inv} = \begin{bmatrix} \rho u \\ \rho u^2 + p \\ \rho uv \\ (\rho E + p)u \end{bmatrix}, \quad \mathbf{G}^{inv} = \begin{bmatrix} \rho v \\ \rho uv \\ \rho v^2 + p \\ (\rho E + p)v \end{bmatrix},$$

$$\mathbf{F}^{vis} = \begin{bmatrix} 0 \\ \Pi_{xx} \\ \Pi_{xy} \\ \Pi_{xx}u + \Pi_{xy}v + Q_x \end{bmatrix}, \quad \mathbf{G}^{vis} = \begin{bmatrix} 0 \\ \Pi_{xy} \\ \Pi_{yy} \\ \Pi_{xy}u + \Pi_{yy}v + Q_y \end{bmatrix}.$$

Here, ρ is the mass density, u and v are the velocity components in x– and y– directions, respectively. E is the total energy density, and p is the static pressure determined by the ideal gas law as

$$p = (\gamma - 1)\left(\rho E - \frac{1}{2}(u^2 + v^2)\right), \tag{3}$$

where γ is the specific heat ratio. The value of γ is considered to be 7/5 for nitrogen gas. The symbols Π_{xx}, Π_{xy}, and Π_{yy} are the components of stress vector $\mathbf{\Pi}$ defined as follows:

$$\Pi_{xx} = -\mu\left[\frac{4}{3}\frac{\partial u}{\partial x} - \frac{2}{3}\frac{\partial v}{\partial y}\right],$$

$$\Pi_{xy} = -\mu\left[\frac{\partial v}{\partial x} + \frac{\partial u}{\partial y}\right],$$

$$\Pi_{yy} = -\mu\left[\frac{4}{3}\frac{\partial v}{\partial y} - \frac{2}{3}\frac{\partial u}{\partial x}\right].$$

The symbols Q_x and Q_y are the heat fluxes in the x– and y–directions, respectively, defined as

$$Q_x = -\kappa\frac{\partial T}{\partial x}, \quad Q_y = -\kappa\frac{\partial T}{\partial y},$$

where T is the absolute temperature. In the above expressions, the symbols μ and κ represent the Chapman–Enskog shear viscosity and the thermal conductivity, respectively. These expressions for the Chapman–Enskog linear transport coefficients can be employed as[39]

$$\mu = \left(\frac{T}{T_{ref}}\right)^s, \qquad \kappa = \left(\frac{T}{T_{ref}}\right)^s, \tag{4}$$

where T_{ref} is the reference temperature. Here, the value of T_{ref} is considered as $T_{ref} = 273.15$ K. The symbol s stands for the index of the inverse power laws of gas molecules, given as

$$s = \frac{1}{2} + \frac{2}{\nu - 1}. \tag{5}$$

Published under license by AIP Publishing

Here, the parameter v is the exponent of the inverse power laws for the gas particle interaction potentials. The value of s is assumed to be 0.78 for nitrogen gas.[48]

C. Numerical method based on mixed-type discontinuous Galerkin approach

Over the past few decades, the discontinuous Galerkin (DG) methods have become popular as an alternative approach for solving the partial differential equations. The DG methods combine the main features associated with the finite element (FE) and finite volume (FV) methods and have been successfully applied to a wide range of applications in gas dynamics, acoustics waves, plasma physics, quantum physics, and magneto-hydrodynamics.[39–46] As a traditional FE method, accuracy is obtained by approximating the solution based on a series of the higher-order polynomials within each element of the domain, rather than employing wide stencils, as in the case of the traditional FV method. However, similar to the FV method, the physics of wave propagation is considered in order to determine the physical solution among multiple solutions at the interfaces of the elements. The DG methods have numerous important features, including hp adaptivity; robustness with strong mathematical properties, well defined for structured/unstructured meshes associated within complex geometries, well suited for non-conforming elements having hanging nodes, very efficient for adopting time-stepping algorithms, and highly parallelizable.

In this study, the compressible NSF equations (2) are solved by an in-house developed explicit mixed-type discontinuous Galerkin solver based on rectangular meshes.[43,44] The computational domain is discretized into rectangular elements, and scaled Legendre polynomial functions are employed for elements. The Gauss–Legendre quadrature rule is implemented for both the volume and the boundary integrations, and the local Lax–Friedrichs (LLF) is applied for the inviscid term,[47] while the local discontinuous Galerkin (LDG) scheme is employed for the auxiliary and viscous fluxes at elemental interfaces.[41] A polynomial expansion of third-order accuracy is used to approximate solutions in the finite element space, and an explicit third-order accurate SSP Runge–Kutta scheme is used for the time integration. To eliminate the spurious numerical fluctuations of the solutions, the nonlinear total variation bounded (TVB) limiter proposed by Cockburn and Shu is used.[42]

III. GRID REFINEMENT AND VALIDATION STUDY

In order to visualize the computational results, we consider the numerical schlieren image based on the magnitude of the gradient of the density field. It is defined as[49]

$$S_{i,j} = exp\left(-k(\phi_{i,j})\frac{|\nabla\rho_{i,j}|}{max_{i,j}|\nabla\rho_{i,j}|}\right), \tag{6}$$

where

$$k(\phi_{i,j}) = \begin{cases} 20 & \text{if } \phi_{i,j} > 0.25, \\ 100 & \text{if } \phi_{i,j} < 0.25. \end{cases}$$

For the numerical simulation, the computational time is considered as non-dimensionalized to produce a dimensionless time scale (τ) defined as

$$\tau = t \cdot \frac{c\,\mathrm{M}_s}{a}, \tag{7}$$

where t is the real computational time, c is the local sound speed, M_s is the Mach number of the incident shock wave, and a is the edge length of the square.

A. Grid refinement study

To evaluate the quality of the computational results, a grid refinement study is carried out by computing two test cases on the

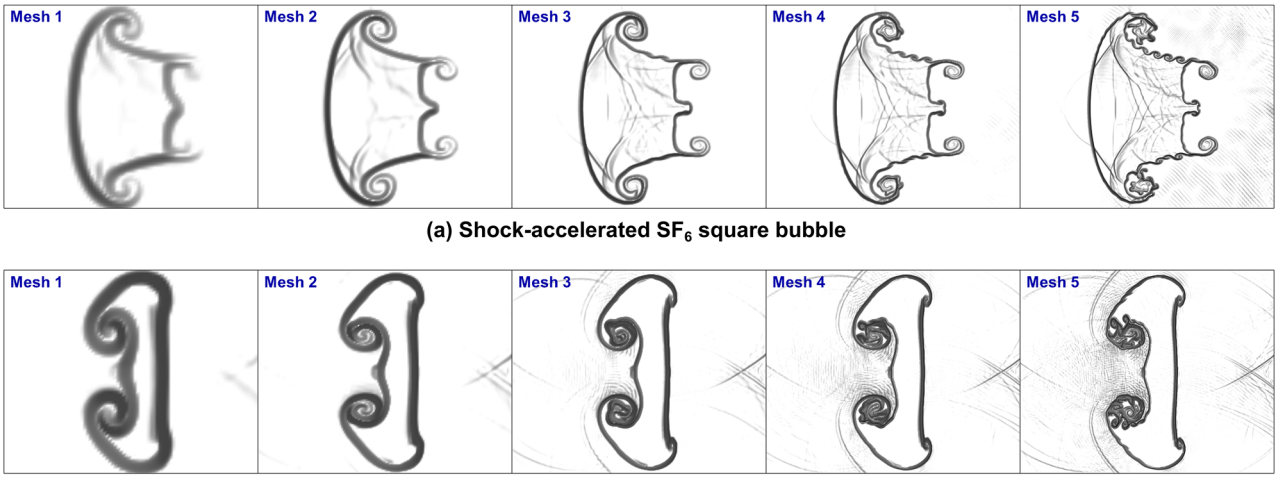

FIG. 2. Grid refinement study: numerical schlieren images with five different meshes points for (a) the shock-accelerated SF_6 square bubble and (b) the shock-accelerated He square bubble at $M_s = 1.21$ and time $\tau = 14$.

Published under license by AIP Publishing

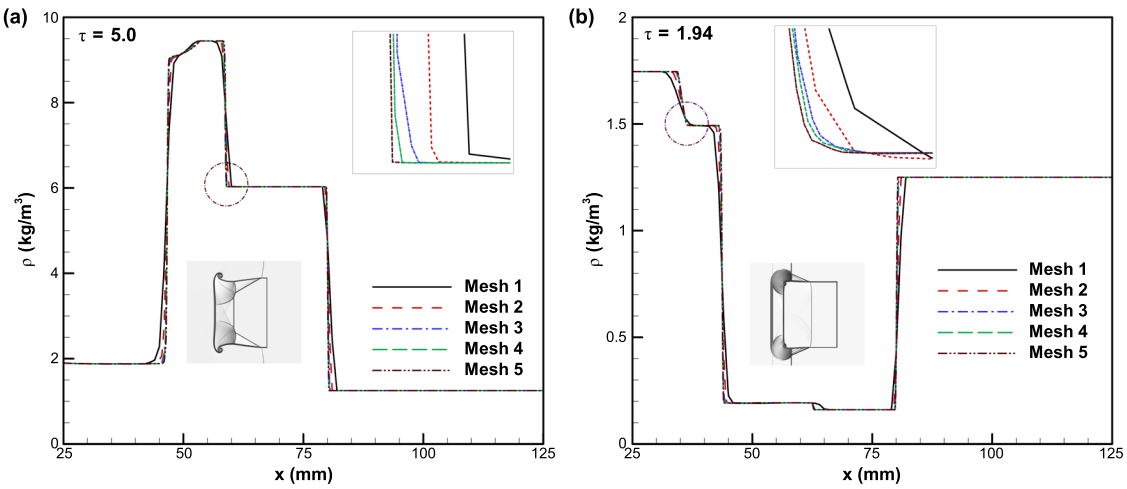

FIG. 3. Grid refinement study: density distribution profiles for different mesh sizes along the centerline of the computed bubble for (a) the shock-accelerated SF_6 square bubble and (b) the shock-accelerated He square bubble.

TABLE I. Comparison of total circulation $\Gamma(m^2/s)$ for selected mesh points at $\tau = 14$.

N_2-bubble configuration	Mesh 1	Mesh 2	Mesh 3	Mesh 4	Mesh 5
N_2–SF_6	−2.044	−2.544	−3.044	−3.850	−3.902
N_2–He	6.168	6.568	7.068	7.925	7.972

shock-accelerated SF_6 and He square bubbles in N_2 gas with M_s = 1.21. A series of five uniform rectangular mesh points is taken into account. The labels "Mesh 1"–"Mesh 5" correspond to mesh points 200 × 100, 400 × 200, 800 × 400, 1200 × 600, and 1600 × 800, respectively. When the incident shock hits the square bubble surface, the volume of the bubble is evidently compressed and the shock waves inside the SF_6 and He square bubbles take on the convergent and divergent shapes, respectively. Figure 2 shows the numerical

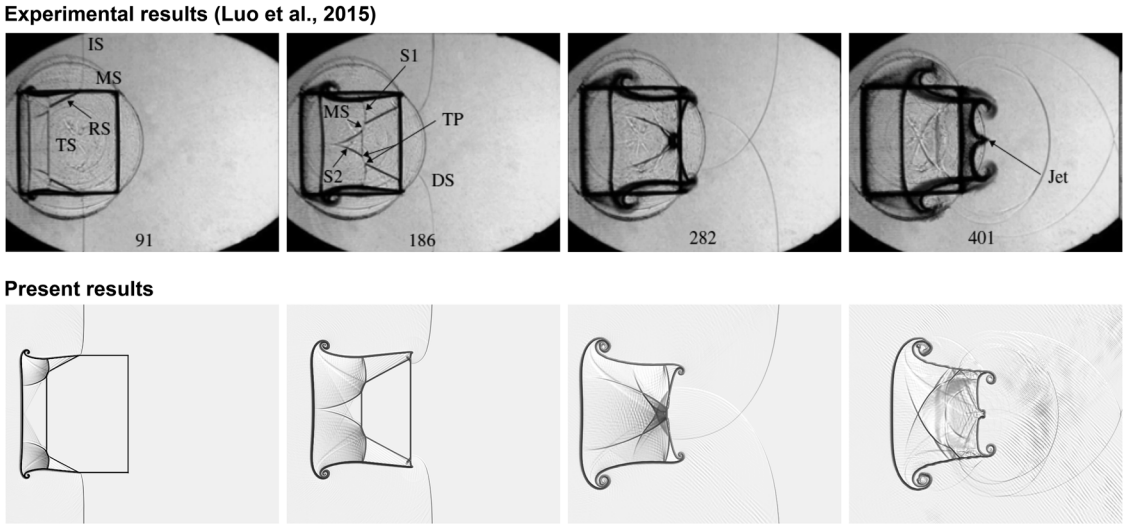

FIG. 4. Validation of the numerical solver: comparison of schlieren images between the experimental results of Luo *et al.*[31] and the present numerical results for an SF_6 square bubble surrounded by air at different time instants.

Published under license by AIP Publishing

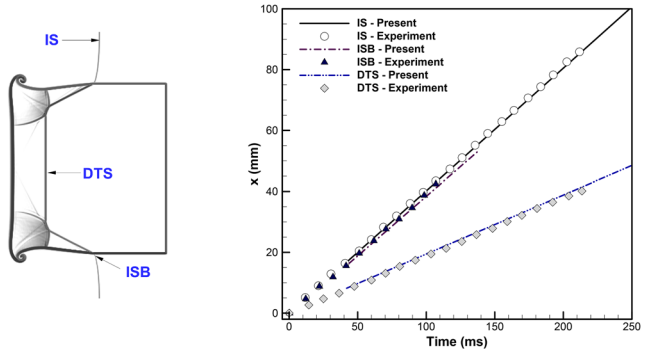

FIG. 5. Validation of the numerical solver: comparison of computed trajectories of the incident shock wave (IS), the incident shock wave along the bubble interface (ISB), and the direct transmitted shock wave (DTS) between the experimental results of Luo *et al.*[31] and the present numerical results for an SF_6 square bubble surrounded by air.

schlieren images for the computed shock-accelerated square bubbles at time $\tau = 14$. The numerical results that the rolled-up of small scale vortices are well captured with "Mesh 5" of mesh points 1600 × 800. Furthermore, the density distribution profiles at the early stage along the centerline of the computed bubbles are also illustrated in Fig. 3 to demonstrate the grid sensitivity. The results show that the "Mesh 5" with mesh points 1600 × 800 is very close to asymptotic range. Table I provides the circulation values for N_2–SF_6 and N_2–He pairing at the computational time $\tau = 14$. The difference between the total circulation values with the "Mesh 4" and the "Mesh 5" is only 0.26%. Based on above-mentioned finding, all the numerical simulations are performed on "Mesh 5."

B. Validation of numerical solver

In order to verify the reliability and accuracy of the present computational model and numerical DG solver, the obtained results are compared with the experimental results of Luo *et al.*[31] where the gas square bubble was filled with SF_6, while the ambient zone was composed of air. The aforementioned experimental studies had a weak shock with $M_s = 1.17$. Figure 4 shows a comparison of the schlieren images between the experimental results of Luo *et al.*[31] and the present numerical results at different times. These numerical simulations share the same initial condition, resolution, wave pattern, and diffusion layer thickness. The present schlieren images show a good degree of agreement with both the experimental and computational results, with the vortex structures resembling one another. In addition, Fig. 5 illustrates a comparison in the trajectories of the incident shock wave (IS), the incident shock wave along the bubble interface (ISB), and the direct transmitted shock wave (DTS). As shown in Fig. 5, the numerically obtained trajectories of these shock waves are very close to the experimental of Luo *et al.*[31]

To further demonstrate the reliability of the present computational method and model, the numerical results of the interaction between a planar shock wave ($M_s = 1.29$) and a two-dimensional N_2 cylinder surrounded by SF_6 are compared with the experimental results of Ding *et al.*[29] Figure 6 shows the comparisons of the

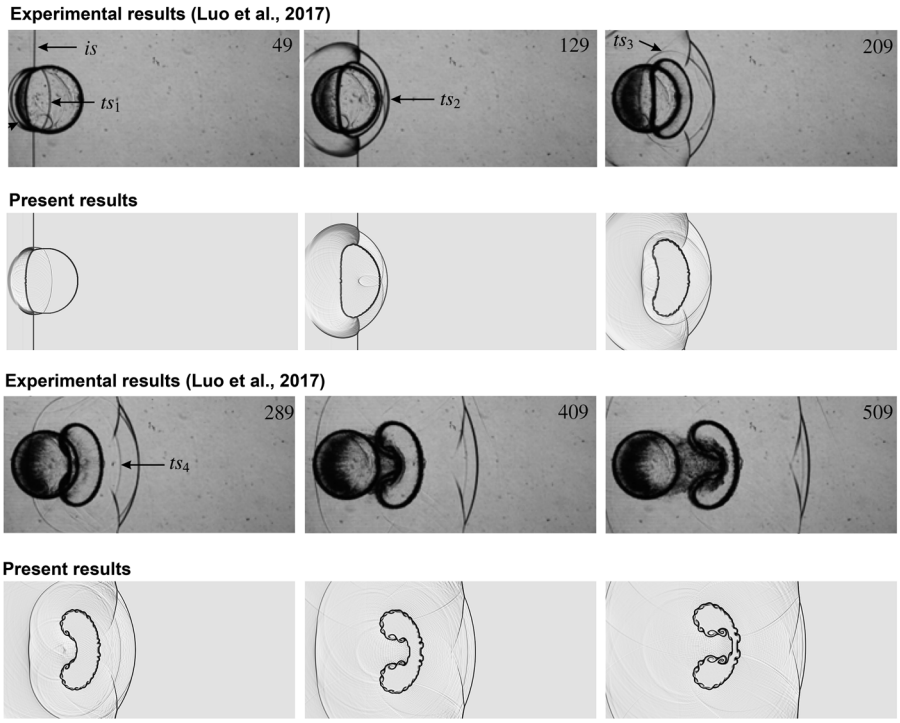

FIG. 6. Validation of the numerical solver: comparison of numerical schlieren images between the experimental results of Ding *et al.*[29] and the present numerical results for a two-dimensional N_2 cylinder surrounded by SF_6 with $M_s = 1.29$ at different time instants.

Published under license by AIP Publishing

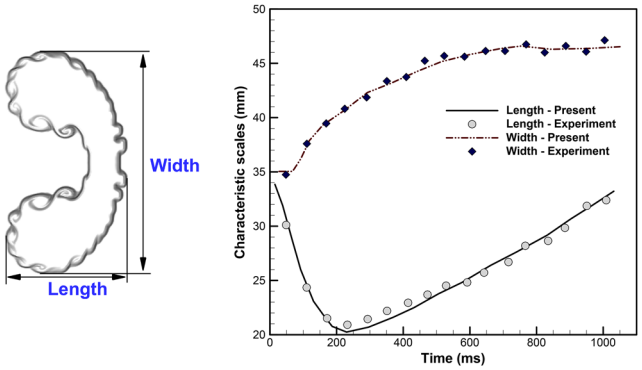

FIG. 7. Validation of the numerical solver: comparison of measured characteristic scales (the length and the width of the evolving interface) between the experimental results of Ding *et al.*[29] and the present numerical results for a 2D N_2 cylinder surrounded by SF_6 with $M_s = 1.29$.

schlieren images between the experimental and the numerical simulation results during the shock-N_2 cylinder interaction at the selected time instants. Good agreement is clearly seen for the evolved shock wave patterns and the cylinder shape at these time instants. Furthermore, the time variations of the interfacial characteristic scales i.e., the length, and the width of the evolving interface for the two-dimensional N_2 cylinder, are also illustrated in Fig. 7. It can be seen from the plot that the present results, including the general trend of the interfacial characteristic scales changing with time, are found very close to the experimental results of Ding *et al.*[29]

IV. RESULTS OF ATWOOD NUMBER IMPACT ON THE SHOCK-ACCELERATED SQUARE BUBBLE AND DISCUSSION

In this section, the impacts of the Atwood number (At) on the flow morphology of the shock-accelerated square bubble are investigated. The impacts of initial interface perturbation on the flow morphology, wave patterns, vorticity distribution, interface movements, and qualitative analysis are emphasized. The incident shock wave with $M_s = 1.21$ is considered for the numerical simulation. Five tested gases inside the square bubble are considered to investigate the impact of the Atwood number—sulfur hexafluoride (SF_6), krypton (Kr), argon (Ar), neon (Ne), and helium (He), while nitrogen (N_2) is considered as the surrounding gas of the square bubble. These gases have been widely adopted in the study of the Richtmyer–Meshkov instability.

This section is divided into five parts: In the first part, the general features of flow morphology of a shock-accelerated square bubble are discussed. In the second part, the flow morphology visualization for selected Atwood numbers are presented. In the third part, the vorticity generation and its related physical phenomena are discussed. In the fourth part, the quantitative analysis based on the shock trajectories, interface features, and integral diagnostics is reported. Finally, a comparative study of flow physics between the shock-accelerated square and cylindrical bubbles is discussed in the last part.

A. General features of flow morphology in a shock-accelerated square bubble

The shock-accelerated bubble is an unsteady flow problem, which results from a planar shock wave passing through a density inhomogeneity of finite size and prescribed shape. The flow morphology for the problem studied here is categorized based on the Atwood number value defined by $At = (\rho_b - \rho_g)/(\rho_b + \rho_g)$, where ρ_b is the density of the bubble and ρ_g is the density of the gas surrounding the bubble. The sign of At determines the configuration of the shock reflection–refraction patterns, which develop during the shock-acceleration process. If the bubble density is greater than the density of the surrounding gas, the value of the Atwood number becomes positive, i.e., $At > 0$, and this scenario represents the "fast-slow" or "heavy-light" configuration. On other hand, if the bubble density is lower than the density of the surrounding fluid, the value of the Atwood number becomes negative, i.e., $At < 0$, and this scenario illustrates the "slow-fast" or "light-heavy" configuration.

Figure 8 represents the schematic diagram of the typical flow morphology for the shock-accelerated square bubble in the "fast-slow" ($At > 0$) and "slow-fast" ($At < 0$) configurations during the early stage of the initial shock wave transit and shortly after the initial shock wave transits. These configurations usually bring out some interesting flow phenomena and processes, including a set of wave configurations associated with the interaction and the deformation of the square bubble interface. When the incident shock wave hits the leftmost surface of the square bubble from the left-hand side, it modifies its uniform front and develops two parts inside the bubble. One part does not directly interfere with the bubble gas, whereas the second part turns into a transmitted wave that interacts with the bubble. In the case of $At > 0$, the transmitted shock travels through the gas bubble more slowly than the incident shock outside the bubble, which is the consequence of the mismatch in acoustic impedances across the bubble surface. Thus, the transmitted shock takes on a convergent shape, whereas in the case of $At < 0$, the scenario is completely different. The transmitted shock travels through the gas bubble faster than the incident shock outside the bubble, and the bubble front attains a divergent shape.

B. Flow morphology visualization

In the study of a shock-accelerated bubble, visualization of the flow evolution is considered a very important tool. To understand the impacts of the Atwood number during the interaction process, we conducted an extensive investigation of the time evolution of the flow morphology in the shock-accelerated square bubble. Hence, five test cases with different values of the Atwood number under the incident and reshock conditions have been considered. The different initial conditions of these five test cases are illustrated in Table II, where the acoustic impedance is obtained by $Z = \rho_b c$ (where ρ_b is the bubble density and c is the sound speed), which indicates the resistance that a pressure wave needs to overcome when it propagates in a certain medium. The evaluated Atwood numbers for N_2-gas square bubble configurations are listed in Table III, where the Atwood number $At > 0$, $At \approx 0$, and $At < 0$ mean the density of the gas bubble is higher, similar, and lower than the density of surrounding gas,

Published under license by AIP Publishing

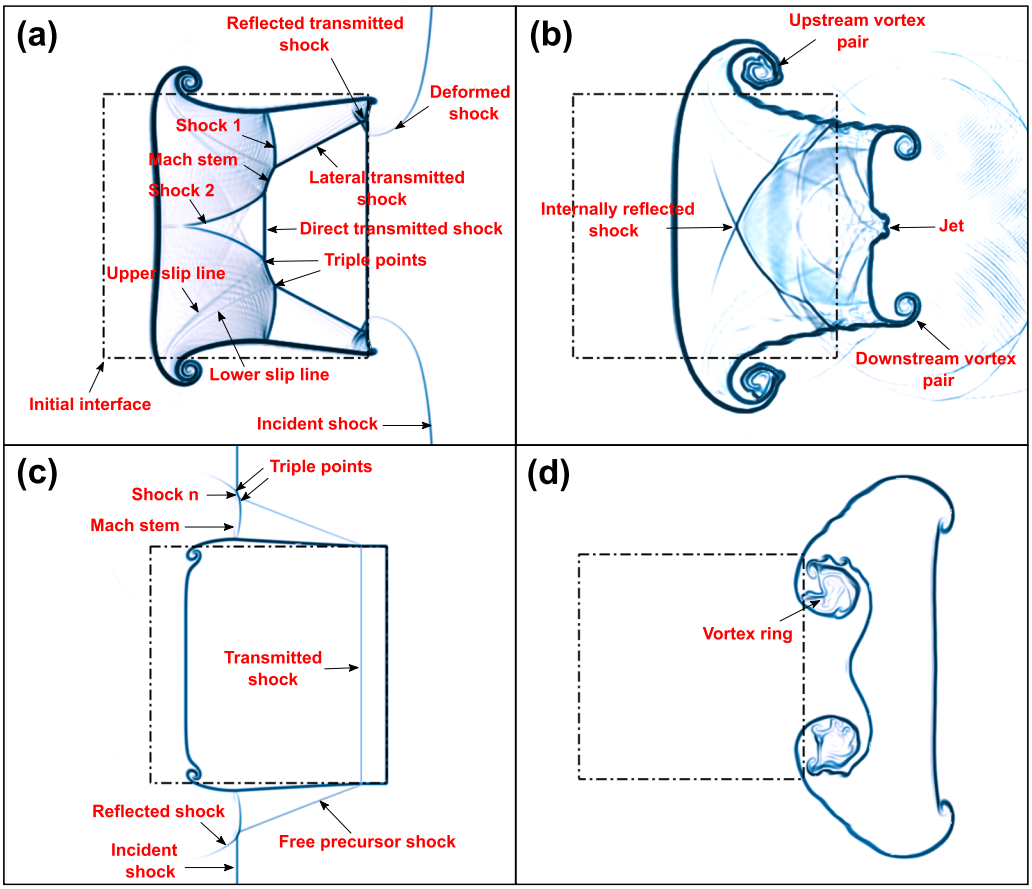

FIG. 8. Schematic diagram of the flow morphology in the shock-accelerated square bubble from the left to right direction. Heavy-light (At > 0) scenario: (a) during transmitted shock transit and (b) shortly after transmitted shock transit. Light-heavy (At < 0) scenario: (c) during transmitted shock wave transit and (d) shortly after transmitted shock wave transit.

respectively, and the values vary from a large positive value to a large negative value, which cover a wide range.

Figure 9 illustrates a sequence of the numerical schlieren images of the square SF_6 bubble in N_2 gas (At = 0.667) accelerated by a planar incident shock wave with M_s = 1.21 at different time instants. The propagation speed of the shock wave inside the SF_6 square bubble is smaller than that of the outside medium due to the larger acoustic impedance (i.e., Z = 814 Pa s/m). The transmitted shock wave inside the bubble is thus situated well behind the planar incident shock (IS) wave outside the bubble. Before interaction with the IS wave, the initial state of the SF_6 square bubble interface can be clearly observed ($\tau = 0$). When the IS wave passes through the square bubble, the frontal and lateral sides of the square bubble are swept (τ = 1.9). The IS wave contracts the frontal region of the gas initial interface (OI), and the trailing region remains intact. A planar direct

TABLE II. Properties of nitrogen and different bubble gas under standard conditions.

Bubble gas	Density (ρ_b) (kg/m^3)	Sound speed (c) (m/s)	Acoustic impedance ($Z = \rho_b c$) (Pa s/m)
SF_6	6.03	135	814
Kr	3.43	222	761
Ar	1.45	319	462
N_2	1.25	352	401
Ne	0.80	452	362
He	0.16	1007	161

TABLE III. Atwood number for N_2—bubble configurations.

N_2—bubble configuration	Atwood number	Flow pattern
N_2–SF_6	0.667	Convergent
N_2–Kr	0.466	Convergent
N_2–Ar	0.074	Convergent
N_2–Ne	−0.218	Divergent
N_2–He	−0.773	Divergent

Published under license by AIP Publishing

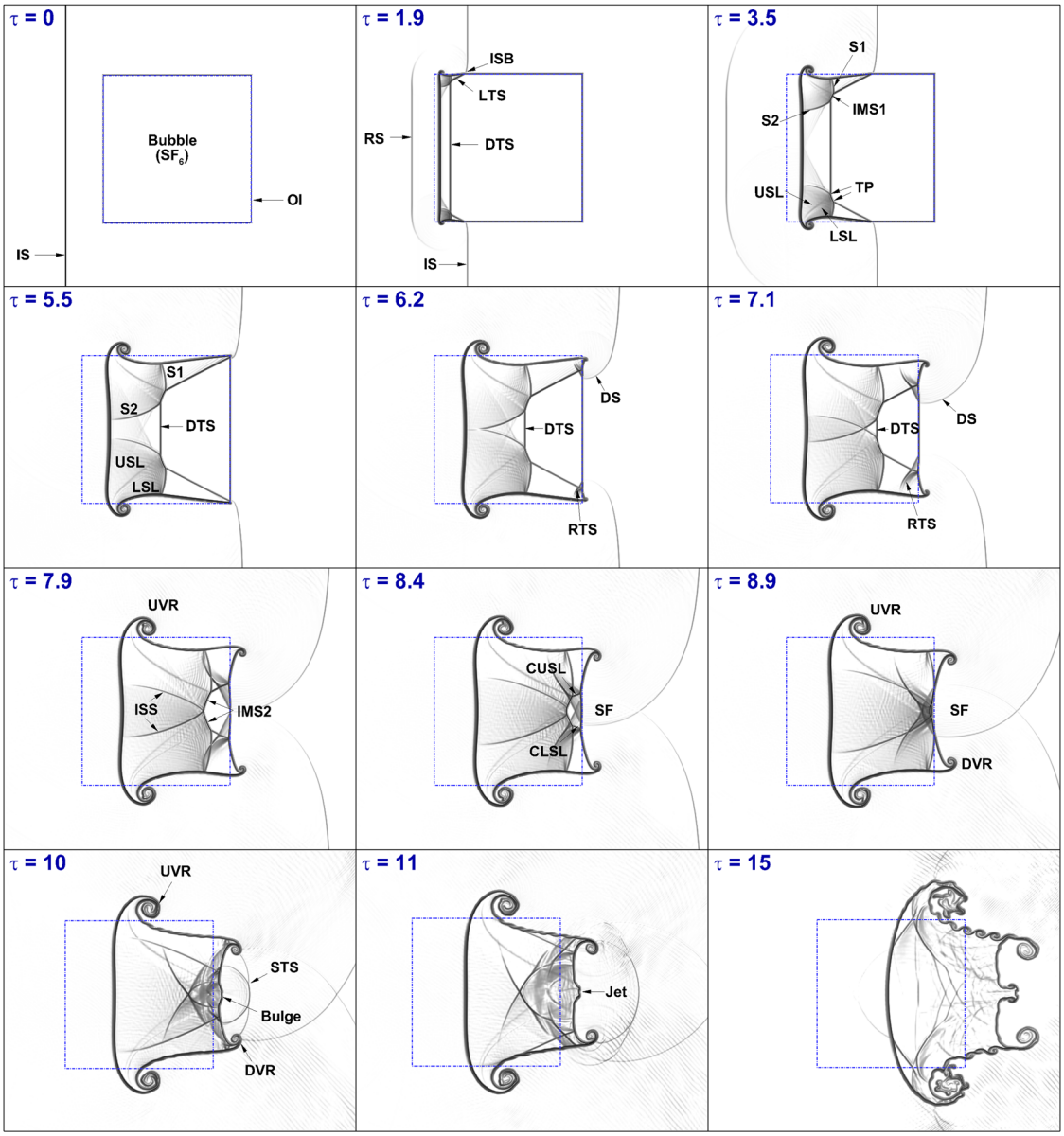

FIG. 9. Time evolution of numerical schlieren images for the shock-accelerated SF_6 square bubble at M_s = 1.21 and At = 0.667.

transmitted shock (DTS) wave is produced after the impact of the IS wave, which apparently travels downstream slower than the IS wave. A lateral transmitted shock (LTS) wave is produced by the IS wave, which sweeps both the top and bottom of the lateral surfaces at a certain angle toward the OI lateral surface. The incident shock wave along the bubble interface (ISB) is also noticed, which travels slower than the IS wave. Besides it, a reflected shock (RS) wave traveling upstream simultaneously is also observed.

As the IS wave propagates along the upper and lower sides of the square, an irregular refraction occurs and the shock–shock interaction between the DTS and LTS waves induces the generation of new shocks (S1 and S2), an internal Mach stem (IMS1), and two triple points (TP) followed by two slip lines—the upper slip line (USL) and the lower slip line (LSL)—inside the bubble (τ = 3.5). As time goes on, the irregular refraction phenomenon is also enhanced (τ = 5.5). When the main part of the IS wave moves ahead of the square, a curved diffracted shock (DS) wave is observed to be connected with the top and bottom ends of the two straight sections of the IS wave (τ = 6.2). Meanwhile, a reversed transmitted shock (RTS) wave is observed inside the leeward corner of the square, which then

Published under license by AIP Publishing

moves upstream simultaneously. As the IS wave passes, the baroclinic vorticity generation (the local pressure and density gradient misalignment) and depositions on the upper and lower interfaces form a small upstream vortex pair (UVR; $\tau = 7.1$). Later, the upper half USL and the lower half LSL are merged, and the triple points move further downstream and separate, leading to the formation of another internal Mach stem (IMS2) and inward secondary shock (ISS) wave ($\tau = 7.9$). This IMS2 and the corresponding two slip lines—the converging upper slip line (CUSL) and converging lower slip line (CLSL)—form a "wedge" structure ($\tau = 8.4$). Besides it, a distinct shock focusing occurs inside the square near the leeward stagnation point due to the DS wave intersecting with each other. The upstream vortex pair (UVR) continuously increases in size over time, and a small downstream vortex pair (DVR) emerges ($\tau = 8.9$). After focusing, the DS wave emerges from the bubble downstream end and a secondary transmitted shock wave (STS) is generated, which expands outward downstream. Subsequently, a bulge with the same width as that of the IMS2 front is generated at the gas interface. Shortly afterward, the bulge moves downstream, and consequently, an outward jet, driven by the peak pressure caused by the complex

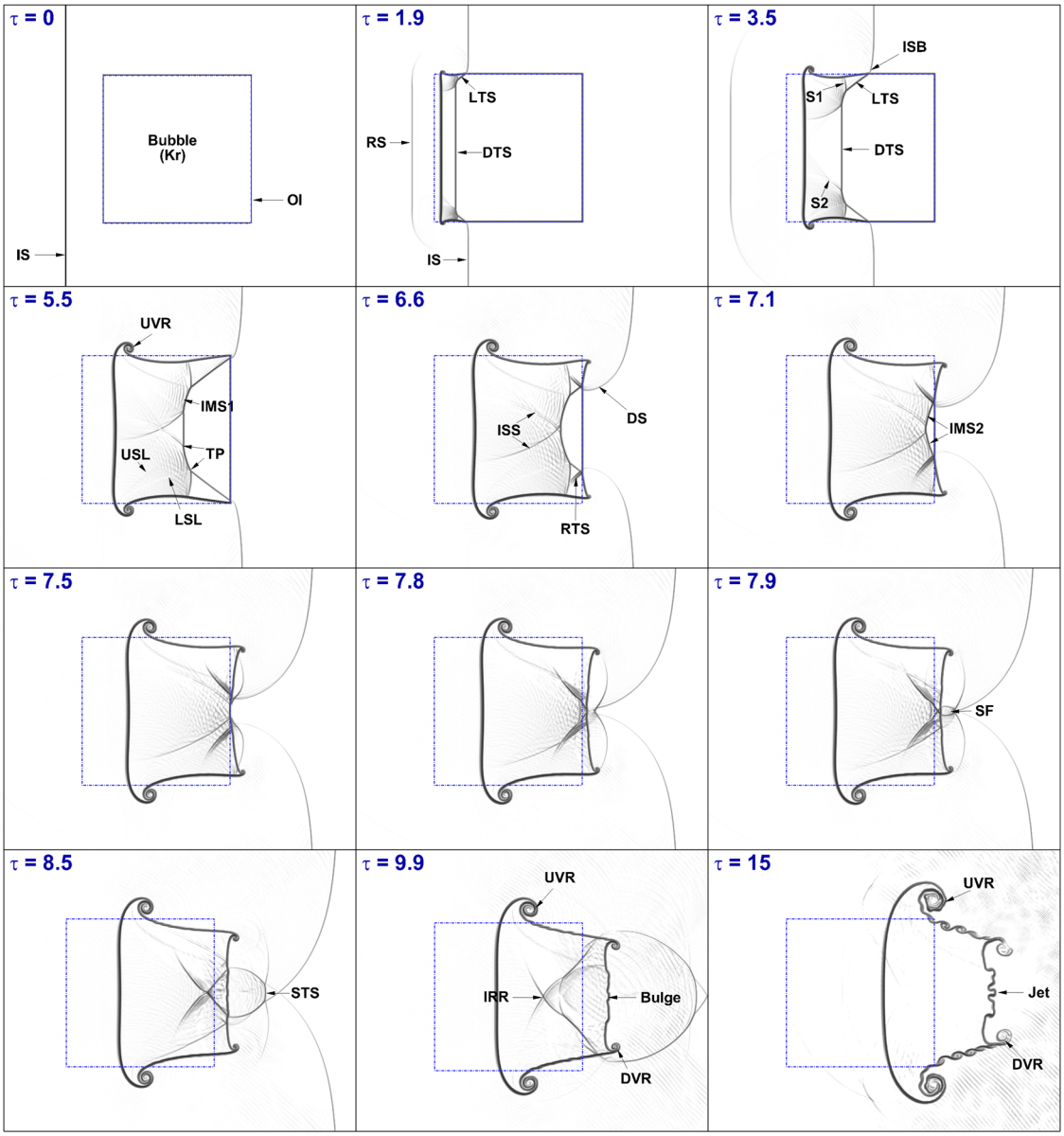

FIG. 10. Time evolution of numerical schlieren images for the shock-accelerated Kr square bubble at $M_s = 1.21$ and At = 0.466.

Published under license by AIP Publishing

interaction among shocks inside the bubble near the downstream boundary, is observed and grows along both vortex pairs UVR and DVR with time (τ = 11–15).

There should be some difference in the flow morphology of the shock-accelerated Kr square bubble, given the gas density and acoustic impedance of Kr are both smaller than those of SF_6, as shown in Table II. In order to study these differences in detail, Fig. 10 shows a sequence of the numerical schlieren images of the square Kr bubble in N_2 gas (At = 0.466) accelerated by a planar incident shock wave with M_s = 1.21 at different time instants. Compared with Fig. 9, the reflected shock (RS) wave can also be seen clearly in the frontal part of square, and the direct transmitted shock (DTS), lateral transmitted shock (LTS), reflected transmitted shock (RTS), diffracted shock (DS), and other shock configurations can also be observed. However, because of the smaller acoustic impedance of Kr than that of SF_6, the shock waves in the Kr square bubble travel faster than in the SF_6 square bubble, and so, the size of the unshocked region in the Kr square bubble is smaller than in the SF_6 square bubble (τ = 3.5–5.5). Then, the focusing of the shock wave takes place during τ = 7.8–7.9, but the shock focusing position is slightly closer to

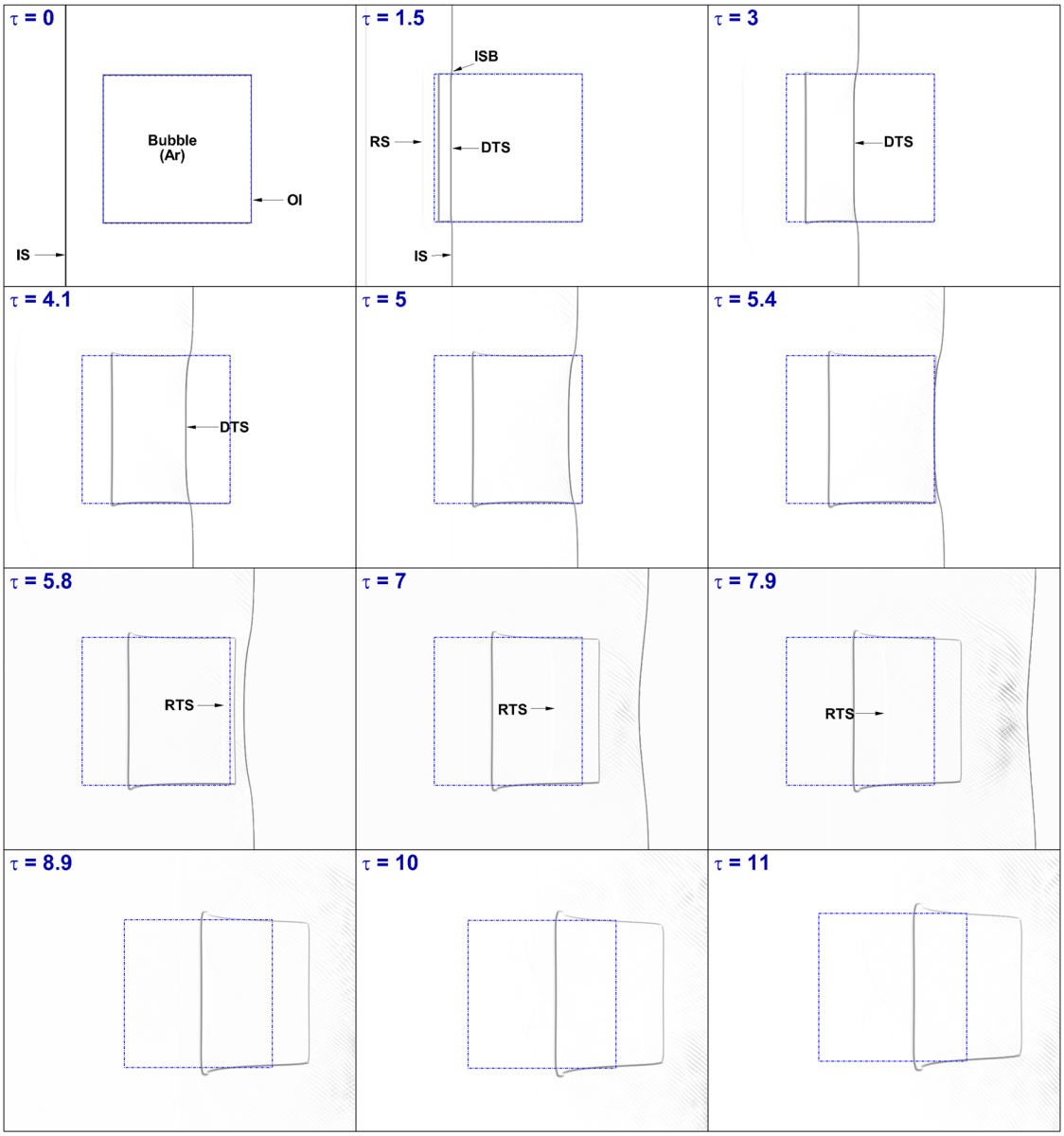

FIG. 11. Time evolution of numerical schlieren images for the shock-accelerated Ar square bubble at M_s = 1.21 and At = 0.074.

Published under license by AIP Publishing

the downstream pole of the Kr square bubble relative to the case of the SF_6 square bubble, and the shock focusing period is also advanced. Unlike the case of the SF_6 square bubble, both upstream and downstream vortex pairs (UVR and DVR) are generated at the corners of the Kr square interface with lower strengths. Interestingly, a different pattern of jet formation is observed at the central part of the rear surface of the Kr square bubble owing to the high pressure resulting from the shock focusing phenomenon (τ = 15). Although there are some specific differences between the two different cases, due to the values of the Atwood number for the Kr and SF_6 gases, the overall trends of the Kr and SF_6 square bubbles in the evolution of shock waves and bubble deformation are basically consistent.

When the density of the square gas bubble continues to decrease, the density of Ar is slightly greater than that of the surrounding nitrogen, which is characterized by a positive value of the Atwood number (At = 0.074). This configuration implies that the shock-accelerated square bubble is still in a "fast-slow" configuration. Figure 11 shows a sequence of numerical schlieren images showing the interaction between an incident shock (IS) wave and

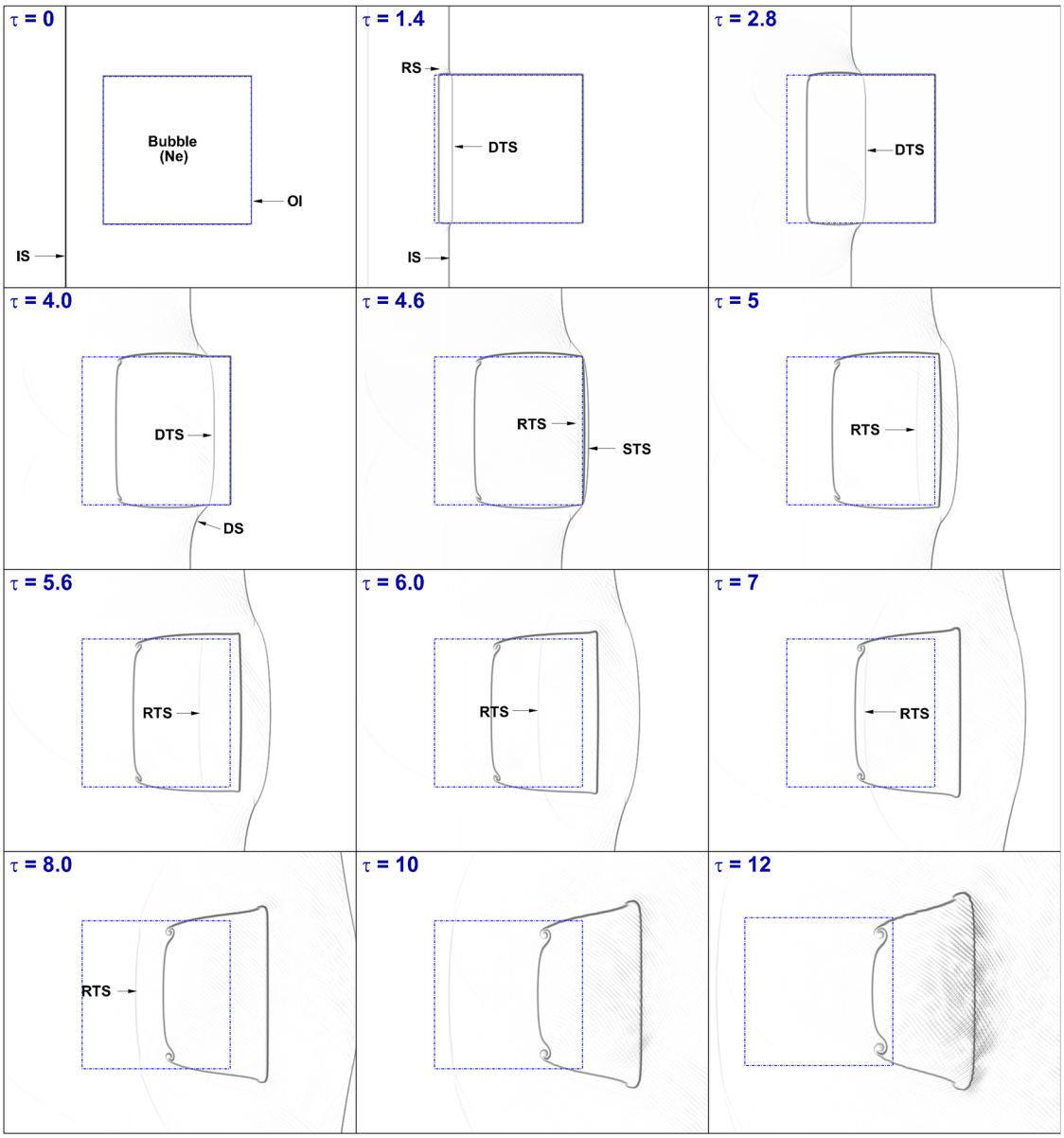

FIG. 12. Time evolution of numerical schlieren images for the shock-accelerated Ne square bubble at M_s = 1.21 and At = −0.218.

Published under license by AIP Publishing

an argon square bubble. As predicted, the resulting wave pattern in this configuration would be different from the one shown with At = 0.667 and At = 0.446 because of the close similarity in the acoustic impedance of the involved gases (nitrogen and argon). Indeed, one can observe in Fig. 11 that the IS and the direct transmitted shock (DTS) waves travel at similar speeds. At the initial stage of the IS wave interacting with the square bubble, the propagation speed of the DTS wave in the bubble is slightly slower than that of the IS wave outside because the acoustic impedance of Ar gas is slightly greater than that of N_2. At the same time, it is also observed that due to the interaction between the IS wave and the bubble, a reflected shock (RS) wave is generated near the left interface of the square bubble. As the IS wave propagates, the RS wave propagates to the top and the bottom of the flow field continuously. It is observed that the DTS into the Ar bubble reaches the bubble rear surface almost at the same time as the IS wave reached this location. Once the DTS shock wave within the square bubble reaches the rear surface of the bubble, a shock wave is transmitted into the ambient N_2 gas and a reflected transmitted shock (RTS) wave is generated inside the bubble. This RTS wave later exits the

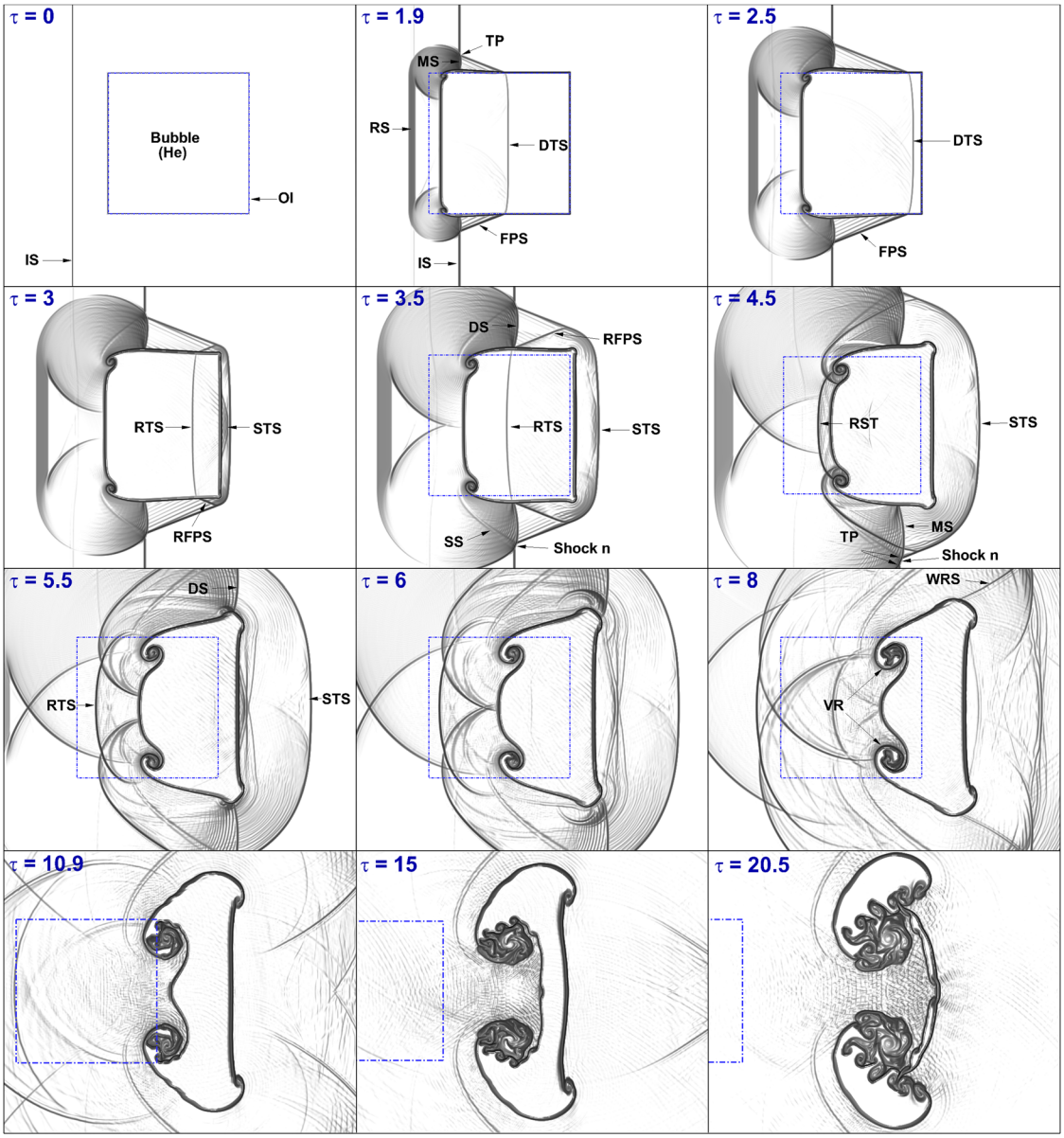

FIG. 13. Time evolution of numerical schlieren images for the shock-accelerated He square bubble at M_s = 1.21 and At = −0.773.

Published under license by AIP Publishing

bubble from its frontal surface and proceeds to propagate upstream into the nitrogen gas. Different bubble deformation at At = 0.074 is visible relative to the results obtained at At = 0.667 and At = 0.446, as shown in Figs. 9 and 10. Interestingly, no vortex pair is generated at the frontal corners of the initial square bubble due to generated weaker shock wave from the bubble frontal surface. However, the bubble frontal corners are slightly bent outward during the investigated time.

As the density of the square gas continues to fall, the density of Ne is slightly lower than that of the surrounding N_2, distinguished by a negative value of the Atwood number (At = −0.218). This configuration means that the shock-accelerated square bubble is in a "slow-fast" configuration. Figure 12 illustrates a sequence of numerical schlieren images of the square Ne bubble accelerated by a planar IS wave with M_s = 1.21. At the beginning of the IS wave hitting the square bubble, the propagation speed of the direct transmitted shock (DTS) wave inside the bubble is much higher than that of the IS outside the bubble because the acoustic impedance of Ne gas is slightly smaller than that of nitrogen gas (τ = 1.51–2.95). At the same time, it is observed that the IS and bubble collision creates a reflected shock (RS) wave near the left bubble interface. As the interaction proceeds, the Ne square bubble starts to compress, and both left–most interface corners slightly begin to bend due to the baroclinic vorticity (τ = 4.09). Similar to the Ar case, as the DTS hits the rear surface of a square bubble, it transmits a shock (STS) wave into the ambient N_2 gas and it produces a reflected transmitted shock (RTS) wave (τ = 4.56). After then, the STS wave is merged into a straight plane in front of the bubble, while the RTS exits the bubble from its frontal surface and proceeds to propagate upstream into nitrogen gas. In the case of At = −0.218, a completely different bubble deformation is observed from the previous results obtained with all positive Atwood numbers, as illustrated in Figs. 9–11. Over time, the frontal corners of the bubble are gradually more bent inward, and the rear corners of the surface are also slowly starting to bend.

Finally, helium (He) gas is considered as the fifth gas in our shock-accelerated square bubble computation. Figure 13 presents the numerical schlieren images of the time evolution of the square He bubble in N_2 (At = −0.773) accelerated by a planar incident shock wave with M_s = 1.21 at different time instants. When the incident shock (IS) wave travels along the upper and lower boundaries, and the transmitted shock (TS) wave within the square bubble moves significantly faster than the IS wave outside the bubble. Also, a reflected shock (RS) wave propagating upwards is generated outside the square interface (τ = 1.9). The TS wave is itself refracted at the bubble interface and transmits a new oblique shock wave, the so-called free precursor shock (FPS), in the ambient gas. The FPS and IS waves

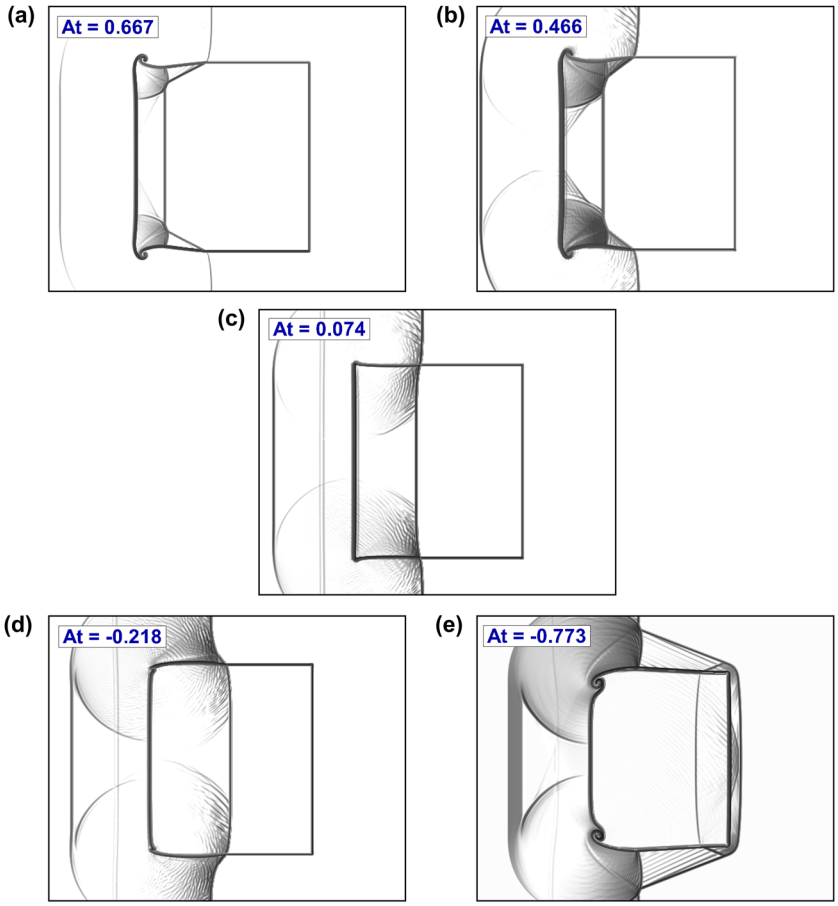

FIG. 14. Impacts of the Atwood number on a shock-accelerated square bubble at the same early stages: numerical schlieren images for (a) At = 0.667, (b) At = 0.466, (c) At = 0.074, (d) At = −0.218, and (e) At = −0.773 at τ = 3.

Published under license by AIP Publishing

are then joined together and mutually modified, producing a triple point (TP), a Mach stem (MS), and a shock outside the bubble. Two small vortices are observed at the left corners of the square interface due to the vorticity deposition (τ = 2.5). When the TS wave inside the bubble encounters the downstream interface, a secondary transmitted shock (STS) wave traveling downward is produced and seen ahead of the original IS wave (τ = 3). Then, a reflected transmitted shock (RTS) wave inside the He bubble is produced at the upstream surface and is moving now in the opposite direction toward the bubble's front. A new shock wave called reflected free precursor shock (RFPS) is generated and connected between the RTS wave from the bubble rear surface and the FPS wave. This RFPS wave propagates toward the bubble frontal surface. A diffracted shock wave (DS) is also produced, moving along the rightmost surface (τ = 3.5). Once the RTS wave within the bubble reaches the bubble front, it transmits into the surrounding gas in front of the bubble (τ = 4.5). The shocks reflected from the shock tube wall (WRS) are also clearly seen at (τ = 8), which can affect the interface height and the vorticity production. The impact of the incident shock wave on the interface evolution is decreased as time goes on and the vortex pair at the corners gradually grows, caused by the produced vorticity (τ = 10.9–15). The flow field is completely controlled by the vortex pair at later times (τ = 20.5).

For comparative analysis of the different Atwood number effects on the shock-accelerated square bubble, the numerical schlieren images at the same early stages τ = 3 and the same shock strength M_s = 1.21 are considered in Fig. 14. For each Atwood number, the deformation of the square bubble during the penetration of the incident shock wave is determined by the density and acoustic impedance. The slowest speed of penetration is observed in SF_6 and Kr, and this speed is, at the same time, slower than the normal incident shock wave. In these cases, the transmitted shock travels through the square bubbles more slowly than the incident shock outside the bubbles boundary. The transmitted shock in the SF_6 square bubble moves also more slowly than in the Kr square bubble. This situation is different in the case of the Ar square bubble, where a slight difference between the speeds of transmitted and incident shock waves results in a smaller deformation of the bubble. The case of Ne and He exemplifies a scenario opposite to that for the SF_6 and Kr gases. The fastest speed of penetration is observed in the He bubble, and this speed is, at the same time, faster than the normal incident shock. Figure 15 illustrates the relation between the displacement of the direct transmitted shock (DTS) wave and the Atwood number at time τ = 3. It is observable that as the Atwood number goes toward positive values and becomes larger, the DTS wave propagates through the bubble more slowly.

Figure 16 shows the impacts of the Atwood number on the pressure distributions at two different time instants τ = 2 and 6. The pressures are displayed along the centerline of the computed bubble with M_s = 1.21. As seen from the pressure profile, the fastest shock propagation inside the bubble is observed at At = −0.773, while the slowest shock propagation is noticed at At = 0.667. The largest pressure jump is witnessed at At = 0.667, while the smallest pressure jump is observed at At = −0.773. At the early stage τ = 2, the pressure jump across the DTS wave in the case of At = 0.667 is noticed as 1.5 times of the value in At = −0.773, as shown in Fig. 16(a). The pressure jump is fairly uniform during the

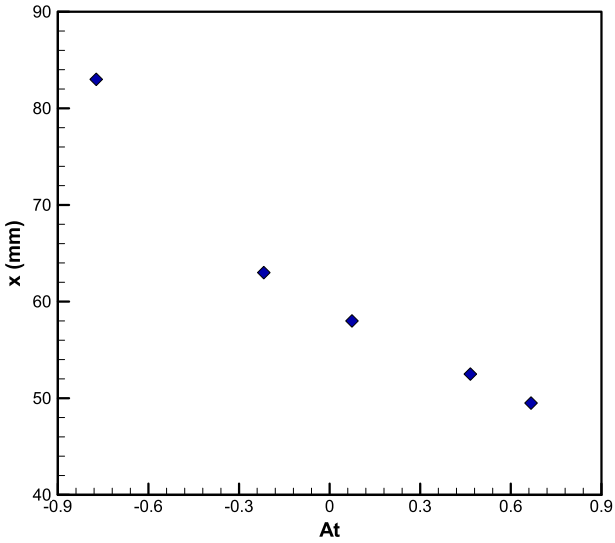

FIG. 15. Impacts of the Atwood number on the displacement of the direct transmitted shock (DTS) wave at τ = 3.

investigated time for all Atwood values except from At = −0.773. Due to the shock reflection from the He square bubble interface, the pressure state behind the propagating IS wave starts to be nonuniform, as seen at x = 42–52 mm in Fig. 16(a). At time τ = 6, the pressure state behind the propagating shock wave is clearly nonuniform for all Atwood numbers due to multiple shock reflections from the bubble's interface, as illustrated in Fig. 16(b). The direct transmitted shock (DTS) wave inside the bubble travels downstream toward the square bubble rear surface, while the reversed transmitted shock (RTS) wave from the square bubble frontal interface continues to travel upstream into the surrounding N_2 gas for At = 0.074, −0.218, and −0.773, as shown in Figs. 11–13. In the case of At = 0.466, a sudden pressure change behind the DTS wave front is observed at x = 72 mm due to the concentration of the compression wave in this region, as shown in Fig. 10. In the case of At = −0.733, the flow morphology is observed to be more complex. At x = 43 mm and τ = 6, the RTS wave from the bubble rear surface has already reached the bubble frontal surface and emerges into the surrounding N_2 gas, as shown in Fig. 13. The other secondary transmitted shock (STS) wave at x = 112 mm continues to move downstream, as shown in Fig. 16(b).

Furthermore, this comparative analysis can be extended to visualize the evolution of the square bubble shape during interaction with the IS wave at different Atwood numbers, as shown in Fig. 17. The bubble appears to be compressed by the IS wave along the x−direction, and its top and bottom edges have been pushed forward near the horizontal axis of symmetry as compared to its middle section. At the beginning of interaction, this compression starts as soon as the IS wave hits the upstream end of the bubble. For At > 0, the downstream interface hardly moves, while the upstream side presses forward under the influence of the IS wave at the early instants, as shown in Figs. 17(a)–17(c). As time goes on, the upper and lower interfaces of the bubble also fold forward toward the axis,

Published under license by AIP Publishing

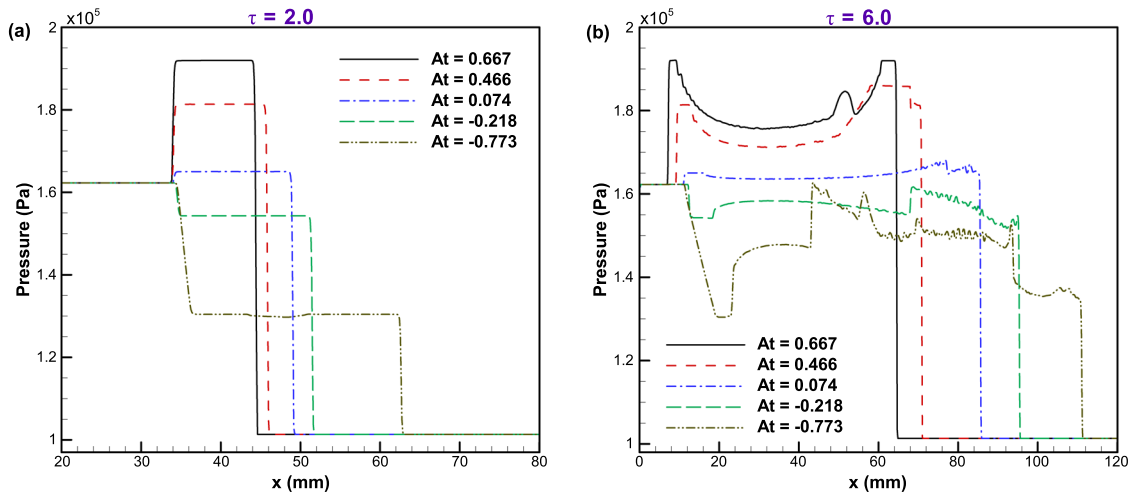

FIG. 16. Impacts of the Atwood number on the pressure distribution obtained along the centerline of the computed square bubble at two different instants: (a) τ = 2.0 and (b) τ = 6.0.

and the bubble takes the convergent shape. A small upstream vortex pair (UVR) is created on the upper and lower interfaces due to the baroclinic vorticity generation, particularly for At = 0.667 and At = 0.466. The UVR is continuously increasing over time, and a small downstream vortex pair (DVR) is also emerging at the corners of downstream interface. Later, an outward jet and an inward jet are observed near the downstream boundary at At = 0.667 and At = 0.466, respectively, and expand along with both vortex pairs UVR and DVR with time, as shown in Figs. 17(a) and 17(b). In the case of At = 0.074, the IS and the direct transmitted shock (DTS) waves travel with the similar speeds. Therefore, no vortex pair is observed at the frontal corners of the initial square bubble. However, as time passes, the bubble frontal corners are slightly bent outward, as shown in Fig. 17(c). On the other side, for At < 0, the both upstream and downstream interfaces travel fast, and the upstream side presses inward under the influence of the IS wave at the early instants, as shown in Figs. 17(d) and 17(e). When time goes, two small vortices are observed at the left corners of the square interface due to the vorticity deposition. The impact of the IS wave on the interface evolution as time goes on and the vortex pair at the corners gradually grow. At later times, the flow field is completely controlled by the vortex pair.

C. Vorticity generation

In the study of a shock-accelerated square bubble, the vorticity occurring due to the misalignment of the pressure and the density gradients plays a vital role in understanding the flow morphology phenomena during the interaction process. When the incident shock wave crosses the bubble, vorticity is generated in the flow field. It can be expressed as the curl of the velocity

$$\omega = \nabla \times \mathbf{u}. \tag{8}$$

The role of the acoustic impedance mismatch in the creation of a vorticity field can be explained based on the vorticity transport equation, which includes several physically distinctive quantities. This equation can be obtained by taking the curl of the momentum equation for a compressible flow, given as

$$\frac{\partial \omega}{\partial t} = (\omega \cdot \nabla)\mathbf{u} - \omega(\nabla \cdot \mathbf{u}) + \frac{1}{\rho^2}(\nabla\rho \times \nabla p) + \frac{\mu}{\rho}\nabla^2\omega, \tag{9}$$

where ω, ρ, $\mathbf{u}$, p, and μ represent the vorticity, density, velocity, pressure, and shear viscosity coefficient, respectively. On the right-hand side of Eq. (7), the term $\omega(\nabla \cdot \mathbf{u})$ represents the fluid convection and thermal expansion, which is only appropriate for highly compressible fluids. The term $(\omega \cdot \nabla)\mathbf{u}$ represents the vortex stretching, which is critical for the 3D turbulence and mixing discussion. The term $(\mu/\rho)\nabla^2\omega$ represents the acceleration due to the diffusion of velocity. Finally, the term $(1/\rho^2)$ $(\nabla\rho \times \nabla p)$ denotes the baroclinic vorticity decomposition, which is responsible for the production of small-scale rolled-up vortices at the bubble interface. Let us analyze closely the impact of the baroclinic vorticity term as the incident and refracted shocks pass the stationary square bubble interface in the early stage of evolution. At the leftmost vertical interface, where the pressure and density gradients are perfectly aligned, a small quantity of vorticity (rolled-up vortex) is generated at the corners (top and bottom) when the incident shock touches them. As the incident shock propagates along the horizontal upper interface, Mach reflection occurs in which the Mach stem (MS) connects the IS wave with the square interface. Therefore, the MS contributes the pressure gradient for the vorticity generation on the interface, and the baroclinic vorticity term is thus triggered gradually as the incident shock travels upwards over the square interface. Interestingly, the downstream end of a heavy gas bubble interface grows less rolled-up vortices compared to the downstream end of a light gas bubble interface. The schematic diagrams of the vorticity generation on the interfaces of the square bubble after initial shock wave transit in heavy (At > 0) and light (At < 0) gas bubbles are illustrated in Fig. 18.

Published under license by AIP Publishing

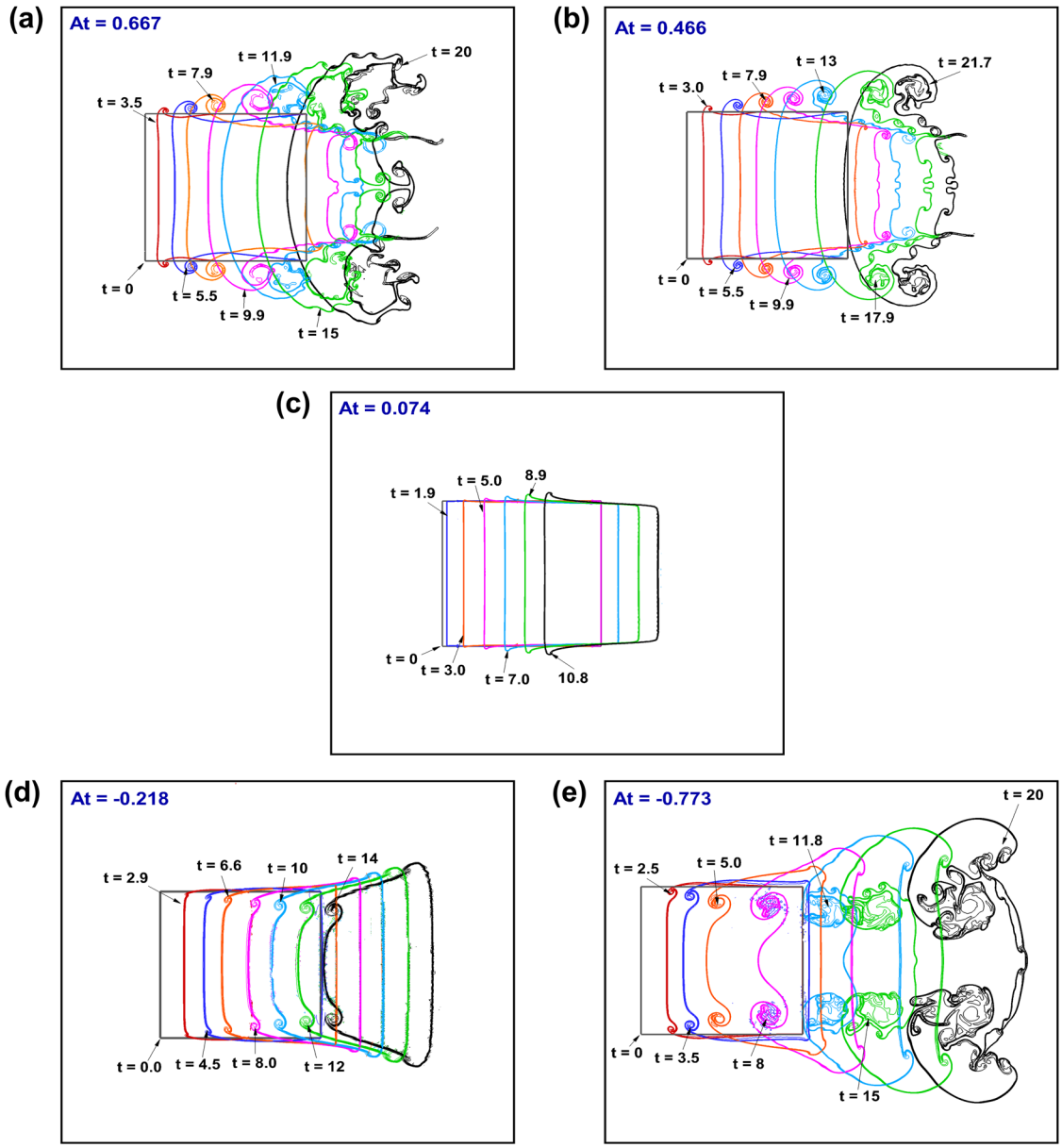

FIG. 17. Impacts of the Atwood number on a shock-accelerated square bubble: evolution of the bubble shape showing early compression for (a) At = 0.667, (b) At = 0.466, (c) At = 0.074, (d) At = −0.218, and (e) At = −0.773.

It is well known that the key factor leading to growth in the initial disturbance is the deposition of baroclinic vorticity (i.e., misalignment of the gradients of pressure and density) with the interface of the bubble. To illustrate the impacts of the Atwood number on the vorticity distribution in the shock-accelerated square bubble, the vorticity contours at several time instants are shown in Fig. 19. It is observed that there are significant differences in vorticity distribution for the different Atwood numbers after the interaction. In the case of the positive Atwood number (At > 0), it can be observed that significant quantities of negative and positive vorticity are generated on the upper and lower interfaces of the square bubble, as shown in Figs. 19(a)–19(c). A great amount of vorticity is found in both the upper and lower vortex pairs (UVR and DVR) at the corners of the square interface. Moreover, the deformed shock wave produces a small quantity of negative and positive vorticity on the upper and lower interfaces after shock focusing, and the dominant positive (negative) vorticity is also gathered on the upper-half (lower-half) plane in the outward jet head, particularly at At = 0.667 and

Published under license by AIP Publishing

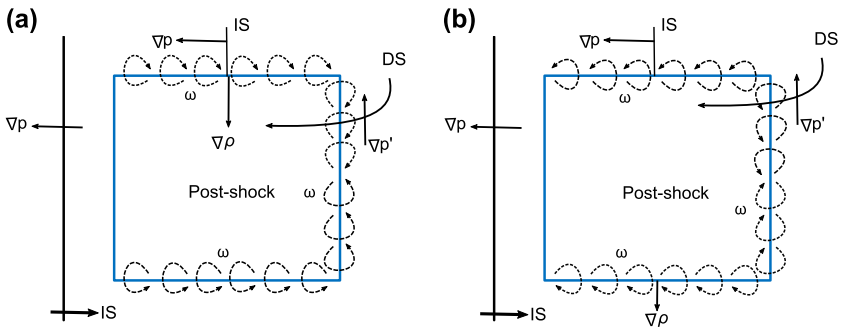

FIG. 18. Schematic diagrams of the vorticity generation on the boundaries for the square bubble after initial shock wave transit in (a) the heavy gas bubble (At > 0) and (b) light gas bubble (At < 0). The ∇p-pressure gradient caused by the incident shock wave; $\nabla p'$-pressure gradient caused by the diffracted shock wave.

At = 0.466. The potential explanation for the gathering of dominant positive (negative) vorticity in the outward jet head on the upper-half (lower-half) plane is the higher amplitude attenuation of the deformed shock wave when it hits the downstream pole of the bubble. This positive (negative) vorticity on the upper (lower) jet head promotes outward jet movement, which implies the relationship between the jet formation and the vorticity deposition.

In the case of At ≈ 0 i.e., At = 0.074, which still follows the "fast–slow" configuration, it may be observed that there is no vorticity generation in the leftmost and rightmost vertical interfaces of the square bubble. Interestingly, in the case of a negative Atwood number (At < 0), the positive vorticity is generated on the upper horizontal side of the bubble and the negative vorticity is generated on the lower horizontal side of the bubble, as shown in Figs. 19(d) and 19(e). This is because of the IS wave propagating from left to right along the bubble interface. As a result, the density gradient is everywhere radially outwards at the bubble interface, and the pressure gradient is across the upstream IS wave. Furthermore, the vortical structure in the upper interface is observed with positive vorticity at the center, surrounded by tails of negative vorticity, while vice versa situations are noticed in the bottom interface of the square bubble.

D. Quantitative analysis

In order to investigate the impacts of the Atwood number on the shock-accelerated square bubble, a quantitative analysis is presented here based on the physical phenomena of the shock trajectories, the interface features, and the integral diagnostics (i.e., the enstrophy, the average vorticity, and the dissipation rate).

1. Shock trajectories and interface features

Figure 20 illustrates the trajectories of the incident shock (IS) wave, the incident shock wave along the bubble interface (ISB), and the direct transmitted shock (DTS) wave computed for all prescribed At values in the square bubble. It can be noticed that the fastest waves are found in the case of At = −0.773 (He gas), while the slowest waves are seen in the case of At = 0.667 (SF_6 gas). Interestingly, in the case of the At > 0 value, the velocity of the ISB wave is always higher than of the DTS wave and less than that of the IS wave, as shown in Figs. 20(a)–20(c). Since the difference in the acoustic impedance between Ar and N_2 for At = 0.074 is small, i.e., Z = 61 Pa s/m from Table II, the difference between the IS and ISB wave is also small to be observed in Fig. 20(c). However, in the case of At < 0 value, the fastest is the DTS wave and the slowest is the IS wave, as shown in Figs. 20(d) and 20(e).

Figure 21 shows the impacts of the Atwood number on the temporal variations of the interfacial characteristic scales (i.e., the height and the length of the evolving interface) for the computed square bubble. The definitions of the height and the length of the evolving interface are inserted in the diagram. The interface height increases constantly due to the continuous rotation of the vortex pair until the wall reflected shock waves strike the interface and reduce the interface height growth rate. As shown in Fig. 21(a), the maximum interface height is observed in the case of At = −0.773, while the minimum interface height is witnessed for At = 0.074. On the other hand, the interface length decreases due to the shock compression at early stage for all At values, as shown in Fig. 21(b). After the compression phase, the interface length is almost constant for a long evolving time. In the case of At = 0.667 and At = 0.466, the interface length decreases until τ = 6, and then, it increases slowly due to the growing the jet and upstream vortex pairs (DVR), as also shown in Figs. 9 and 10. For the remaining At values, the interface length decreases slowly until τ = 7 and then remains fairly constant.

2. Integral diagnostics

The physical phenomena of vorticity generation during the interaction can be explained by measuring the time evolution of the enstrophy. The time evolution of the enstrophy can be defined as the area integral of the square of the vorticity in the flow field,

$$\text{Enstrophy}(t) = \int_D \omega^2 dxdy, \tag{10}$$

where D is the area of the computational domain.

Figure 22 depicts the effects of the Atwood number on the time evolution of enstrophy in the interaction between the incident shock wave and the square bubble. It can be observed that the values of the enstrophy increase for all Atwood number except the Ar case (At = 0.074) when the incident and reflected shock waves collide with the bubble. For the He case (At = −0.773), the enstrophy increases even faster when the reflected shock wave interacts with the distorted bubble again ($15 \le \tau \le 20$). A reason behind is that the density of the He bubble is significantly smaller than that of the surrounding gas, and thus, the He bubble travels the fastest along with the shock wave under the impingement among the five cases, which increase the time period when the incident shock wave interacts with the

Published under license by AIP Publishing

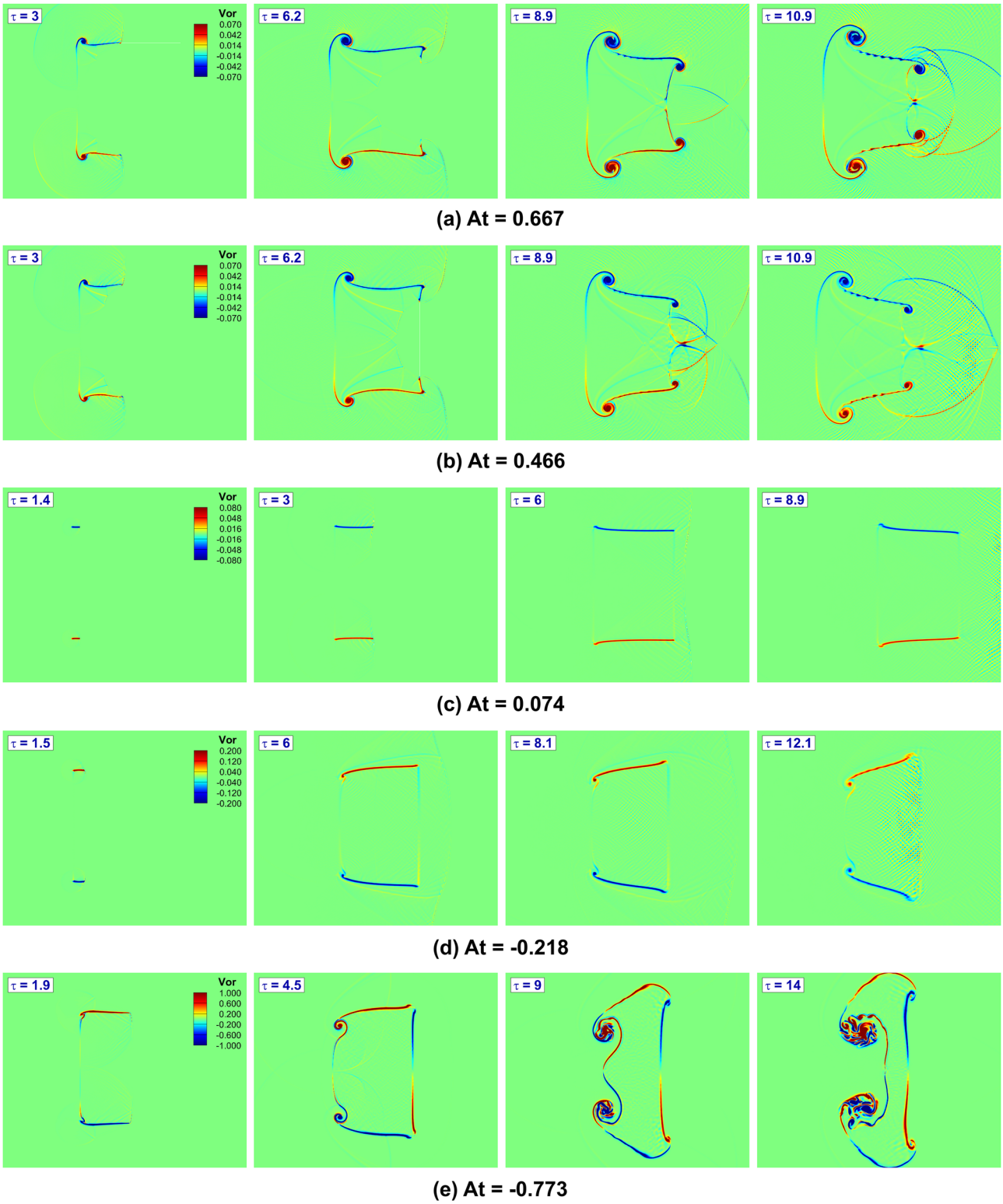

FIG. 19. Impacts of the Atwood number on the shock-accelerated square bubble: contours of vorticity distribution at different time instants for (a) At = 0.667, (b) At = 0.466, (c) At = 0.074, (d) At = −0.218, and (e) At = −0.773.

Published under license by AIP Publishing

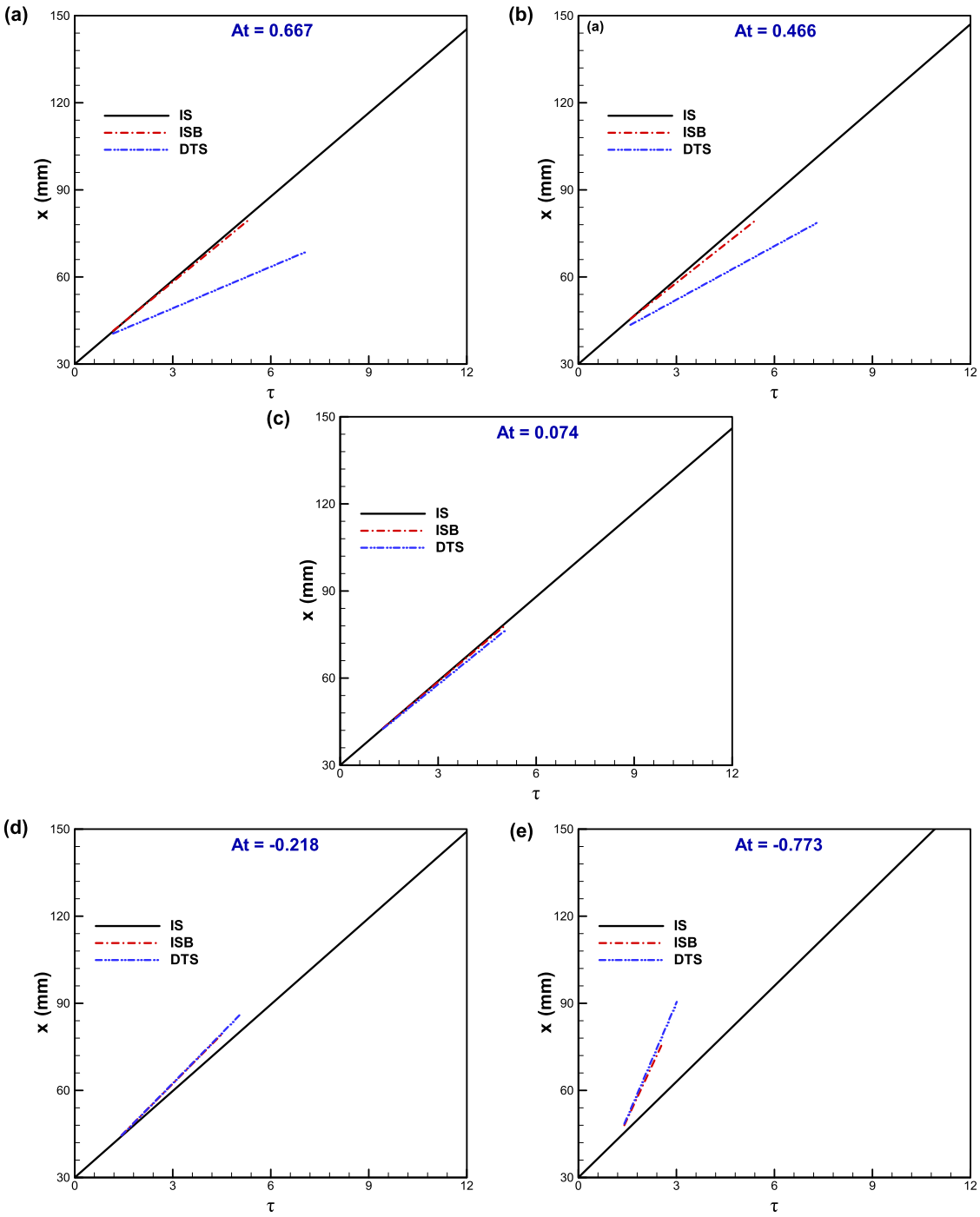

FIG. 20. Impacts of the Atwood number on the shock trajectories (IS, ISB, and DTS) for the computed square bubble for (a) At = 0.667, (b) At = 0.466, (c) At = 0.074, (d) At = −0.218, and (e) At = −0.773.

square bubble to an extent. It is also observed that the time period of an incident shock wave interacting with the bubble is continuously shortened as the Atwood number decreases except for At = −0.773. Furthermore, as expected, enstrophy evolution is observed almost constant for the Ar case (At = 0.074) as the density and acoustic impedance are almost equal for the Ar and N_2 gases. Thus, it can be inferred that evolution of the enstrophy is not merely a monotonous relationship to the Atwood number.

Published under license by AIP Publishing

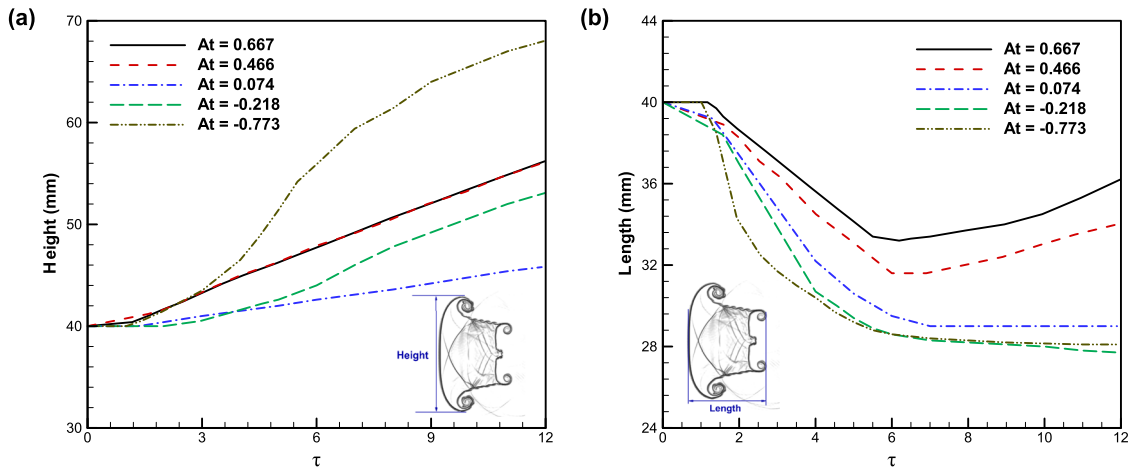

FIG. 21. Impacts of the Atwood number on the temporal variations of the interfacial characteristic scales: (a) the height and (b) the length of the evolving interface for the computed square bubble. The definitions of the height and the length of the evolving interface are inserted.

The vorticity on the bubble interface plays crucial roles in gas mixing inside and outside the bubble, which can be explained via the evolution of the average vorticity in the bubble region. The average vorticity is defined as follows:

$$\text{Average vorticity} = \frac{\int_B |\omega| dxdy}{\int_B dxdy}, \tag{11}$$

where the subscript B represents the bubble region.

Figure 23 illustrates the effects of the Atwood number on the time evolution of the average vorticity during the interaction between the incident shock wave and the square bubble. The values of average vorticity increased with the increase in the Atwood number, specifically for At = 0.667 and At = 0.466, in the "fast-slow" configuration. As the incident and transmitted shock waves affect the square bubbles, the values of the average vorticity rise. The increased vorticity subsequently promotes the mixing of the gases within and outside the bubble, thereby speeding up the transfer and consumption of vorticity energy, which can gradually weaken the average vorticity intensity in the bubble zone. The value of the average vorticity is found constant throughout the whole interaction process at At = 0.074, as shown in Fig. 23. In the case of negative Atwood numbers (At < 0), the average vorticity is observed in an increasing trend when the Atwood number decreases. For At = −0.773, at the stage of

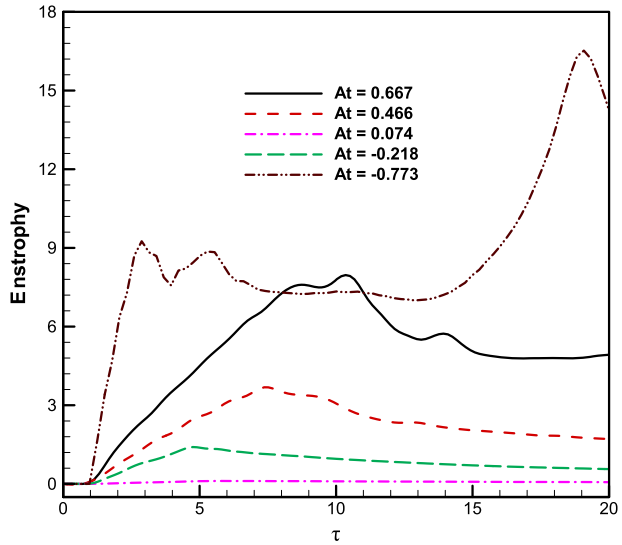

FIG. 22. Impacts of the Atwood number on the shock-accelerated square bubble: time evolution of enstrophy.

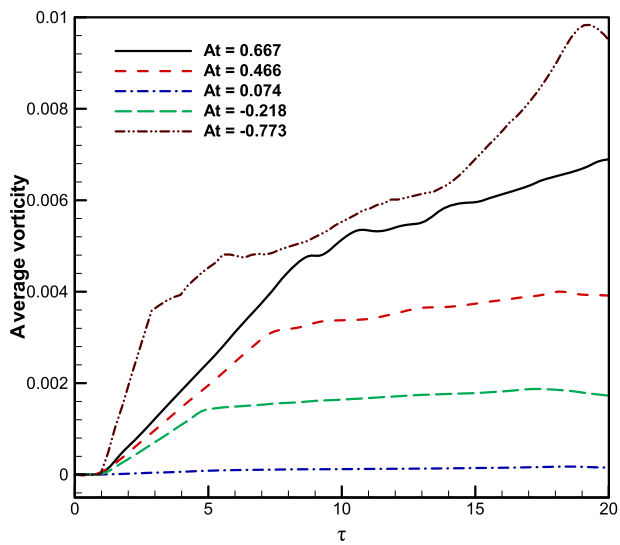

FIG. 23. Impacts of the Atwood number on the shock-accelerated square bubble: time evolution of average vorticity.

Published under license by AIP Publishing

the incident shock wave colliding with the square bubble, the average vorticity is rapidly enhanced, and then, a partial oscillation occurs due to the impingement of the waves within the square bubble. The average vorticity rises at a higher rate as the reflected shock wave hits the distorted He square bubble again and then oscillates under the multi-influences of the collision of the waves within the bubble and the transfer and consumption of vorticity energy.

Furthermore, the impact of the Atwood number on the shock-accelerated square bubble can be investigated by introducing the area-weighted dissipation rate of kinetic energy,

$$\text{Dissipation rate}(t) = \int_{\Omega} E(x, y, t)\,dxdy. \tag{12}$$

Here, $E(x, y, t)$ denotes the dissipation rate per unit volume and is defined as

$$E(x, y, t) = -(\Pi_{xx}S_{xx} + \Pi_{xy}S_{xy} + \Pi_{yx}S_{yx} + \Pi_{yy}S_{yy}), \tag{13}$$

where Π_{ii} is the viscous shear stress and S_{ij} is the strain rate defined as $S_{ij} = \partial u_i/\partial x_j$. Figure 24 shows the impacts of the Atwood number on the time evolution of the dissipation rate in a shock-accelerated square bubble at $M_s = 1.21$. It can be clearly seen that the value of the dissipation rate is diminished as the positive Atwood number decreases, while a reversed trend is observed for a negative Atwood number.

E. Comparative study of the flow physics between the shock-accelerated square and cylindrical bubbles

A comparative study of the flow physics between the shock-accelerated square and cylindrical bubbles is presented here. For this purpose, two different Atwood numbers—At = 0.667 and At = −0.773—are considered, according to filled bubble gases (SF_6 and N_2), while N_2 gas is assumed as the ambient gas of the bubbles. All numerical simulations are performed with the same Mach number—$M_s = 1.21$.

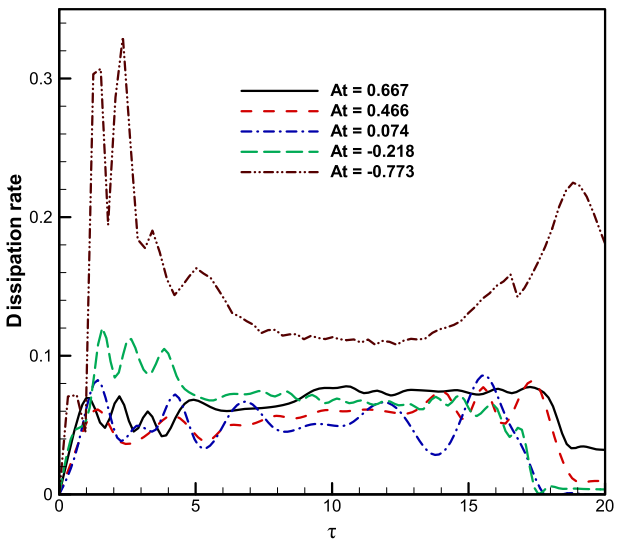

FIG. 24. Impacts of the Atwood number on the shock-accelerated square bubble: time evolution of the dissipation rate.

Figure 25 illustrates a series of the numerical schlieren images for the comparison between the flow morphology of the shock-accelerated SF_6 square and cylindrical bubbles in N_2 gas (At = 0.667) at several time instants. In both bubbles, the propagation speed of the IS wave is smaller than that in surrounding gas due to the large acoustic impedance $Z = 814$ Pa s/m. As a result, the generated DTS wave inside the bubble travels slower behind the IS wave, and the bubbles take the convergent shape. In the case of the square bubble, as shown in Fig. 25(a), when the IS wave passes through the square bubble, a LTS wave is produced along the DTS wave, which apparently travels downstream ($\tau = 3.5$). Moreover, a RS wave traveling toward upstream and an irregular refraction are also observed. As time goes on, the upper and lower interfaces form an upstream vortex pair (UVR) due to the baroclinic vorticity ($\tau = 8.4$). The UVR continuously increases in size over time, and a small downstream vortex pair (DVR) also emerges ($\tau = 10$). During the interaction, a bulge occurs, which expands outwards downstream and takes the form of an outward jet ($\tau = 15$). On the other hand, a different shock wave pattern is found in the case of the cylindrical bubble, as shown in Fig. 25(b). It is found that the circular interface does not have a straight transmitted shock front. After the IS wave touches the upstream interface, the bubble begins to compress, and a regular reflection initially occurs at the circular surface ($\tau = 3.5$). As time goes on, a curved DS wave is seen to be connected with the top and bottom ends of the two straight sections of the IS wave ($\tau = 8.4$). It is noticed that after the DTS wave crosses the bubble, the part of the bubble–ambient gas interface behind it is thicker than the undisturbed interface in front of it. This is because of the roll-up of small scale vortices that are produced by the baroclinic vorticity. A shock-focusing (SF) zone is also observed toward the downstream end point of the bubble on its axis due to the converging the DTS and DS waves. After focusing, the DS wave emerges from the bubble downstream end and a secondary transmitted shock (STS) wave is generated, which expands outwards ($\tau = 10$). Subsequently, the size of rolled-up vortices increases, and they appear conspicuously at the bubble interface. As time goes on ($\tau = 15$), an outward jet is formulated in the centerline at the downstream end of the bubble.

Figure 26 depicts a series of the numerical schlieren images for the comparison between the flow morphology of the shock-accelerated He square and cylindrical bubbles in N_2 gas (At = −0.773). It is shown that the propagation speed of the IS wave is higher than that in surrounding gas due to the small acoustic impedance $Z = 161$ Pa s/m in both bubbles. Therefore, the generated DTS wave inside the bubble travels faster behind the IS wave and the bubbles take the divergent shapes. A different flow morphology from the square bubble is observed in the case of shock-accelerated He cylindrical bubble, as shown in Fig. 26(b). As the interaction develops, the IS and DTS waves form a quadruple shock nature in gas that reveals an irregular refraction ($\tau = 1.9$). As the consequence, a Mach reflection configuration is generated with Mach step (MS), triple point (TP), and free precursor shock (FPS). When the DTS wave cross the bubble region, a secondary transmitted shock (STS) is observed near the downstream interface. Also, a reflected

Published under license by AIP Publishing

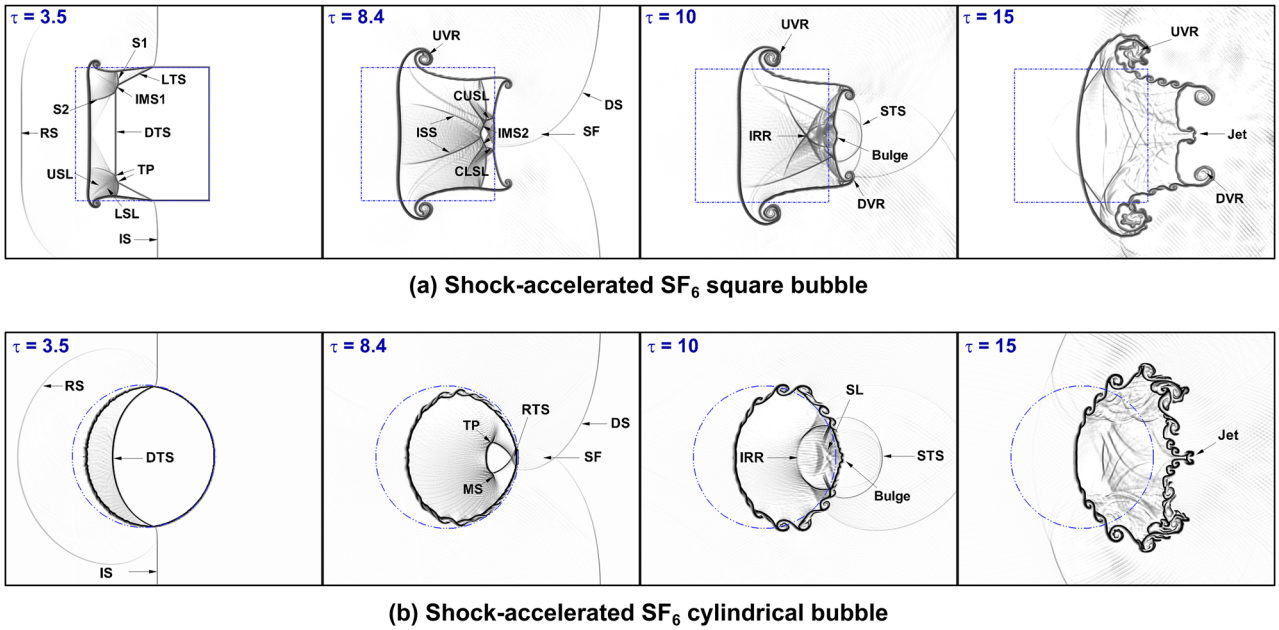

FIG. 25. Comparison of the flow morphology between the shock-accelerated SF_6 square and cylindrical bubbles: numerical schlieren images for (a) the square bubble and (b) the cylindrical bubble with At = 0.667 at several time instants.

transmitted shock (RTS) wave propagating toward the upstream interface of the bubble is produced due to the difference in acoustic impedance of the internal and external gases (τ = 3.5). As time proceeds, the RTS wave moves upwards and then hits the upstream interface, generating a third transmitted shock (TTS) wave (τ = 7). Simultaneously, the flow fields become more complicated near the downstream interface and the bubble is deformed gradually during the interaction. Later, the evolving bubble interface starts to

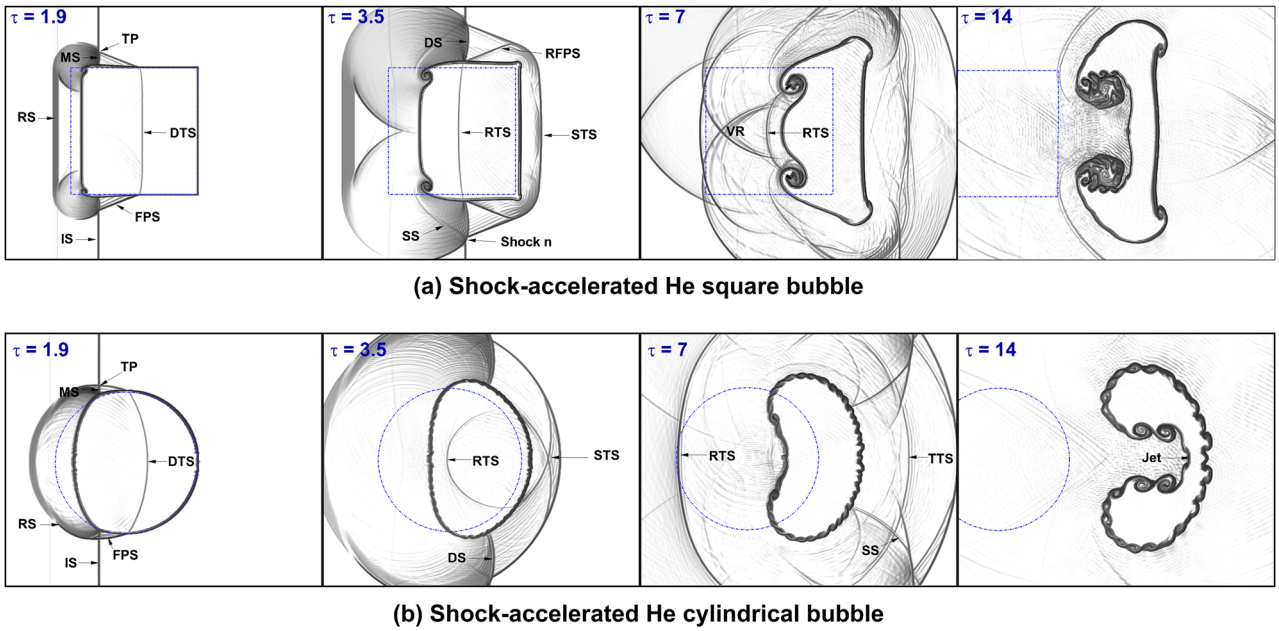

FIG. 26. Comparison of flow morphology between the shock-accelerated He square and cylindrical bubbles: numerical schlieren images for the (a) square bubble and (b) cylindrical bubble with At = −0.773 at several time instants.

Published under license by AIP Publishing

transform into a mushroom shape, and a re-entrant gas jet head is subsequently generated near the center of the bubble (τ = 14). As time goes on, the jet catches up with the downstream bubble interface, and then, a pair of vortex rings connected with a bridge emerge and grow almost symmetrically.

Figure 27 shows the contours of vorticity distribution for the comparison between the shock-accelerated SF_6 square and cylindrical bubbles in N_2 gas (At = 0.667) at several time instants. It is known that the baroclinic vorticity deposition is the main cause of a growth in the initial perturbation at the bubble interface. In both bubbles, based on the direction of the IS wave (from left to right), significant quantity of the negative and positive vorticity is generated on the upper and lower half interfaces of the bubbles, respectively. Interestingly, it is observed that the vortex pairs (UVR and DVR) in the square bubble, and the rolled-up vortices in the cylindrical bubble have a great amount of the negative and positive vorticity. Some amount of the positive and negative vorticity are also noticeable near the vortex pairs and rolled-up vortices in the upper and lower half interface of bubbles. The deformed shock wave produces a small quantity of positive (negative) vorticity on the upper (lower) interface after shock focusing, and the dominant positive (negative) vorticity is also gathered on the upper-half (lower-half) plane in outward jet head. The potential explanation for the gathering of dominant positive (negative) vorticity in the outward jet heads on the upper-half (lower half) plane is the higher amplitude attenuation of the deformed shock wave when it hits the downstream pole of the bubble. This quantity of positive (negative) vorticity on the upper (lower) jet head promotes the outward jet movement, which implies the relationship between the jet formation and the vorticity deposition.

Figure 28 illustrates the contours of vorticity distribution for the comparison between the shock-accelerated He square and cylindrical bubbles in N_2 gas (At = −0.773) at several time instants. In the case of the square bubble, the positive vorticity is generated on the upper horizontal side of the bubble and the negative vorticity is generated on the lower horizontal side of the bubble, as shown in Fig. 28(a). Due to the propagation of the IS wave from left to right along the bubble interface, the density gradient is everywhere radially outwards at the square bubble interface, and the pressure gradient is across the upstream IS wave. In addition, with positive vorticity in the middle, surrounded by tails of negative vorticity, the vortical structure in the upper interface is observed, while vice versa situations are seen in the lower interface of the square bubble, as shown in Fig. 28(a), while in the case of the cylindrical bubble, the positive vorticity is generated on the top side of the bubble and negative vorticity is generated on the bottom side of the bubble, as shown in Fig. 28(b). As time goes on, the vorticity distribution takes a "c-shaped" vortex structure. Due to the interaction of the STS and TTS waves, some amount of negative and positive vorticity is observed in upper and bottom sides of the bubble interface, respectively. In the upper interface of the bubble, the vortical structure has been observed with positive vorticity at the center, surrounded by tails of negative vorticity, while the vice versa situations are noticed in the bottom interface of the bubble.

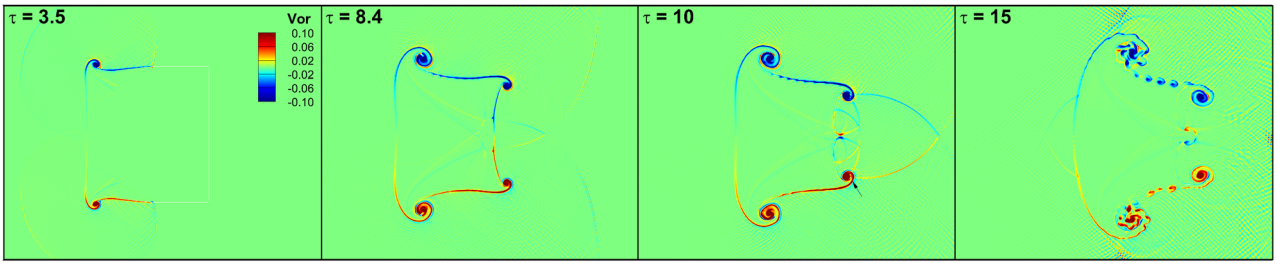

(a) Shock-accelerated SF_6 square bubble

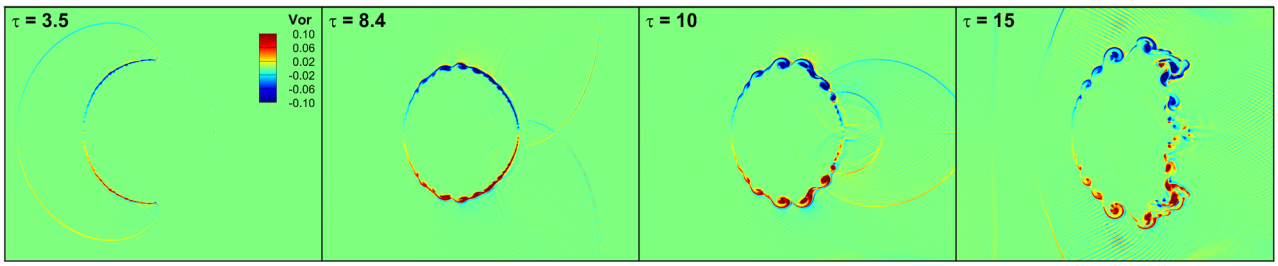

(b) Shock-accelerated SF_6 cylindrical bubble

FIG. 27. Comparison of flow morphology between the shock-accelerated SF_6 square and cylindrical bubbles: contours of vorticity distribution for (a) the square bubble and (b) the cylindrical bubble with At = −0.773 at several time instants.

Published under license by AIP Publishing

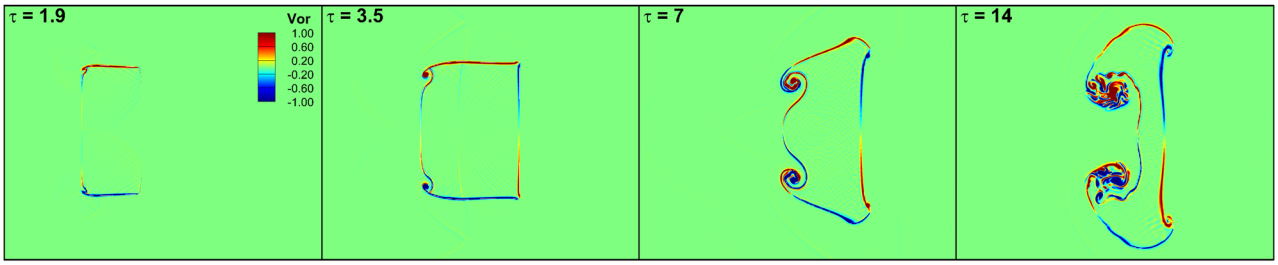

(a) Shock-accelerated He square bubble

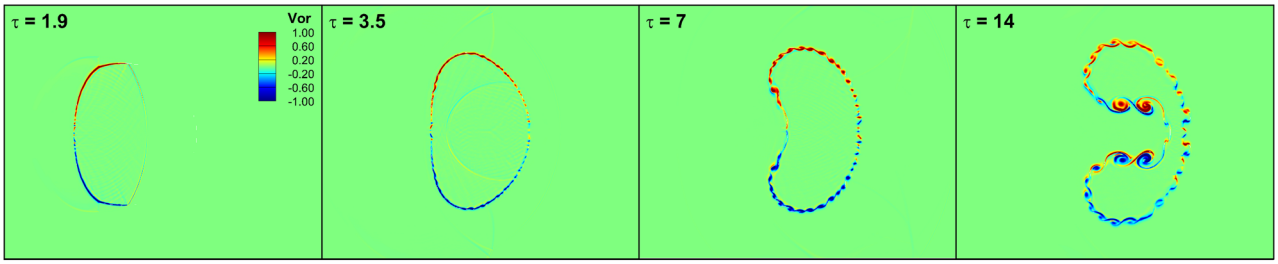

(b) Shock-accelerated He cylindrical bubble

FIG. 28. Comparison of flow morphology between the shock-accelerated He square and cylindrical bubbles: contours of vorticity distribution for (a) the square bubble and (b) the cylindrical bubble with At = 0.667 at several time instants.

V. CONCLUDING REMARKS

The Atwood number plays a critical role for describing the physics of fluids behind the hydrodynamic instabilities such as Richtmyer–Meshkov (RM), Rayleigh–Taylor (RT), and Kelvin–Helmholtz (KH)– in gas dynamics. In this study, the evolution of a shock-accelerated square bubble surrounded by N_2, containing either SF_6, Kr, Ar, Ne, or He, is investigated numerically to determine the impacts of the Atwood number (At). The emphasis is placed on the flow morphology visualization, wave patterns, interface movement and deformation, vorticity generation, and quantitative analysis. For this purpose, the unsteady compressible Navier–Stokes–Fourier equations in two-dimensional spaces are solved by employing an explicit modal discontinuous Galerkin method with uniform meshes. For the validation study, the numerical results are compared by available experimental results and are found to be in good agreement.

The numerical results demonstrate that the Atwood number plays a critical role in describing the RMI instability during the interaction between the shock and square bubble. The impacts of the Atwood number result in a substantial change in the flow morphology with complex wave patterns, vortex creation, vorticity generation, and bubble deformation. To be specific, the main remarkable physical features are summarized as follows:

- For a heavy bubble with At > 0, the speed of the shock wave traveling along with the bubble inner surface is often less than that of the incident shock (IS) wave and greater than that of the direct transmitted shock (DTS) and lateral transmitted shock (LTS) waves. The IS wave focuses near the interior rear surface and generates an inward and outward jet at At = 0.667 and At = 0.446, respectively. It is observed that the shock-focusing time is also advanced when the Atwood number decreases. Interestingly, vortex pairs from the upstream and downstream corners are generated and the upstream vortex pair ultimately dominates the flow morphology.
- For At ≈ 0, the IS wave and the DTS wave travel with very similar speeds. Once the DTS wave reaches the rear surface of the bubble, a shock wave is transmitted into the ambient N_2 and a reflected transmitted shock (RTS) wave traveling upstream is generated within the bubble. Besides it, there is no vortex pair observed at the upstream and downstream corners.
- For a light bubble with At < 0, the transmitted shock wave travels faster than the incident shock wave. A smaller pressure variation is observed, which is in marked difference to the deformation of the investigated bubbles with At > 0. In this scenario, only one vortex pair at the upstream corners is generated, which develops with time and dominates the flow morphology.
- The fastest shock propagation inside the bubble is observed at At = −0.773, while the slowest shock propagation is noticed at At = 0.667. The largest pressure jump is witnessed at At = 0.667, while the smallest pressure jump is observed at At = −0.773.
- For a heavy bubble with At > 0, significant quantities of positive and negative vorticity are generated on the upper and lower interfaces of the bubble, whereas this physical quantity is observed reversed for a light bubble with At < 0.

Published under license by AIP Publishing

- From the viewpoint of quantitative analysis, the time variations of the shock trajectories, the interface scales, and the integral diagnostics are investigated. Interestingly, the maximum interface height is observed at At = −0.773, while the minimum interface height is seen at At = 0.074. The enstrophy evolution during interaction basically shows a non-monotonous relationship to the Atwood number. By contrast, the values of the dissipation rate and average vorticity all decrease as the Atwood number decreases only for At > 0, and the trends are reversed for At < 0.
- A comparative study of the flow physics between the shock-accelerated square and cylindrical bubbles is also presented based on the numerical schlieren images and vorticity contours. Significant different flow features are noticed between square and cylindrical bubbles; in particular, wave patterns, formation of vortex pairs, and vorticity generation on interfaces.

The main goal of the present study is to investigate the impacts of the Atwood number on the flow morphology of the shock-accelerated square bubble containing various light/heavy gases. Interestingly, the bulk viscosity beyond the Stokes's hypothesis plays an essential role in determining non-equilibrium effects in diatomic and polyatomic gases in compressible flows.[43,50] It is also expected that the bulk viscosity will affect significantly the development of the RM instability in compressible fluid flows. Therefore, in this context, the current methodology based on the high-order discontinuous Galerkin method will be extended to investigate the impacts of bulk viscosity on the flow morphology in shock-accelerated polygonal bubbles with different types of interface shapes in future investigations.

ACKNOWLEDGMENTS

The author acknowledges the financial support provided by the Nanyang Technological University, Singapore, through the NAP-SUG grant.

DATA AVAILABILITY

The data that support the findings of this study are available from the corresponding author upon reasonable request.

REFERENCES

[1]R. D. Richtmyer, "Taylor instability in shock acceleration of compressible fluids," Commun. Pure Appl. Math. **13**, 297–319 (1960).
[2]E. E. Meshkov, "Instability of the interface of two gases accelerated by a shock wave," Fluid Dyn. **4**, 101–104 (1969).
[3]J. D. Lindl, R. L. McCrory, and E. M. Campbell, "Progress toward ignition and burn propagation in inertial confinement fusion," Phys. Today **45**(9), 32 (1992).
[4]W. D. Arnett, J. N. Bahcall, R. P. Kirshner *et al.*, "Supernova 1987A," Annu. Rev. Astron. Astrophys. **27**, 629 (1989).
[5]A. R. Jamaluddin, G. J. Ball, and T. G. Leighton, "Shock/bubble interaction near a rigid boundary in shock wave lithotripsy," in 24th International Symposium on Shock Waves (Springer, 2005), pp. 1211-1216.
[6]F. E. Marble, G. J. Hendricks, and E. E. Zukoski, "Progress toward shock enhancement of supersonic combustion processes," in *Turbulent Reactive Flows* (Springer, 1989).
[7]J. Yang, T. Kubota, and E. E. Zukoski, "Applications of shock-induced mixing to supersonic combustion," AIAA J. **31**, 854 (1993).
[8]D. Arnett, "The role of mixing in astrophysics," Astrophys. J. Suppl. **127**, 213 (2000).
[9]M. Brouillette, "The Richtmyer-Meshkov instability," Annu. Rev. Fluid Mech. **34**, 445 (2002).
[10]G. H. Markstein, "A shock-tube study of flame front-pressure wave interaction," in *6th International Symposium on Combustion* (Elsevier, 1957), Vol. 6, p. 387.
[11]G. Rudinger and L. M. Somers, "Behaviour of small regions of different gases carried in accelerated gas flows," J. Fluid Mech. **7**, 161 (1960).
[12]J.-F. Haas and B. Sturtevant, "Interaction of weak shock waves with cylindrical and spherical gas inhomogeneities," J. Fluid Mech. **181**, 41–76 (1987).
[13]J. W. Jacobs, "Shock-induced mixing of a light-gas cylinder," J. Fluid Mech. **234**, 629 (1992).
[14]J. W. Jacobs, "The dynamics of shock accelerated light and heavy gas cylinders," Phys. Fluids A **5**, 2239 (1993).
[15]G. Layes, G. Jourdan, and L. Houas, "Experimental investigation of the shock wave interaction with a spherical gas inhomogeneity," Phys. Fluids **17**, 028103 (2005).
[16]G. Layes and O. Le Métayer, "Quantitative numerical and experimental studies of the shock accelerated heterogeneous bubbles motion," Phys. Fluids **19**, 042105 (2007).
[17]G. Layes, G. Jourdan, and L. Houas, "Experimental study on a plane shock wave accelerating a gas bubble," Phys. Fluids **21**, 074102 (2009).
[18]D. Ranjan, J. H. J. Niederhaus, J. G. Oakley, M. H. Anderson, R. Bonazza, and J. A. Greenough, "Shock-bubble interactions: Features of divergent shock-refraction geometry observed in experiments and simulations," Phys. Fluids **20**, 036101 (2008).
[19]N. Haehn, C. Weber, J. Oakley, M. Anderson, D. Ranjan, and R. Bonazza, "Experimental study of the shock-bubble interaction with reshock," Shock Waves **22**(1), 47–56 (2012).
[20]T. Si, Z. Zhai, J. Yang, and X. Luo, "Experimental investigation of reshocked spherical gas interfaces," Phys. Fluids **24**(5), 054101 (2012).
[21]J. J. Quirk and S. Karni, "On the dynamics of a shock-bubble interaction," J. Fluid Mech. **318**, 129 (1996).
[22]N. J. Zabusky and S. M. Zeng, "Shock cavity implosion morphologies and vortical projectile generation in axisymmetric shock-spherical fast/slow bubble interactions," J. Fluid Mech. **362**, 327–346 (1998).
[23]A. Bagabir and D. Drikakis, "Mach number effects on shock-bubble interaction," Shock Waves **11**(3), 209–218 (2001).
[24]J. H. J. Niederhaus, J. A. Greenough, J. G. Oakley, D. Ranjan, M. H. Anderson, and R. Bonazza, "A computational parameter study for the three-dimensional shock-bubble interaction," J. Fluid Mech. **594**, 85 (2008).
[25]Z. Zhai, T. Si, X. Luo, and J. Yang, "On the evolution of spherical gas interfaces accelerated by a planar shock wave," Phys. Fluids **23**(8), 084104 (2011).
[26]L. Y. Zou, Z. G. Zhai, J. H. Liu, Y. P. Wang, and C. L. Liu, "Energy convergence effect and jet phenomenon of shock-heavy spherical bubble interaction," Sci. China: Phys., Mech. Astron. **58**(12), 124703 (2015).
[27]Y. Zhu, L. Yu, J. Pan, Z. Pan, and P. Zhang, "Jet formation of SF_6 bubble induced by incident and reflected shock waves," Phys. Fluids **29**, 126105 (2017).
[28]Y. Zhu, Z. Yang, K. H. Luo, J. Pan, and Z. Pan, "Numerical investigation of planar shock wave impinging on spherical gas bubble with different densities," Phys. Fluids **31**, 056101 (2019).
[29]J. Ding, T. Si, M. Chen, Z. Zhai, X. Lu, and X. Luo, "On the interaction of a planar shock with a three-dimensional light gas cylinder," J. Fluid Mech. **828**, 289 (2017).
[30]Z. Zhai, M. Wang, T. Si, and X. Luo, "On the interaction of a planar shock with a light polygonal interface," J. Fluid Mech. **757**, 800–816 (2014).
[31]X. Luo, M. Wang, T. Si, and Z. Zhai, "On the interaction of a planar shock with an SF_6 polygon," J. Fluid Mech. **773**, 366–394 (2015).
[32]D. Igra and O. Igra, "Numerical investigation of the interaction between a planar shock wave with square and triangular bubbles containing different gases," Phys. Fluids **30**, 056104 (2018).

Published under license by AIP Publishing

[33]D. Igra and O. Igra, "Shock wave interaction with a polygonal bubble containing two different gases, a numerical investigation," J. Fluid Mech. **889**, 1–20 (2020).
[34]E. Fan, B. Guan, C.-Y. Wen, and H. Shen, "Numerical study on the jet formation of simple-geometry heavy gas inhomogeneities," Phys. Fluids **31**, 026103 (2019).
[35]J. Giordano and Y. Burtschell, "Richtmyer-Meshkov instability induced by shock-bubble interaction: Numerical and analytical studies with experimental validation," Phys. Fluids **18**, 028603 (2006).
[36]S. K. Shankar, S. Kawai, and S. K. Lele, "Two-dimensional viscous flow simulation of a shock accelerated heavy gas cylinder," Phys. Fluids **23**, 024102 (2011).
[37]J. M. Picone and J. P. Boris, "Vorticity generation by shock propagation through bubbles in a gas," J. Fluid Mech. **189**, 23–51 (1988).
[38]R. Samtaney and N. J. Zabusky, "Circulation deposition on shock-accelerated planar and curved density-stratified interfaces: Models and scaling laws," J. Fluid Mech. **269**, 45–78 (1994).
[39]N. T. P. Le, H. Xiao, and R. S. Myong, "A triangular discontinuous Galerkin method for non-Newtonian implicit constitutive models of rarefied and microscale gases," J. Comput. Phys. **273**, 160–184 (2014).
[40]L. P. Raj, S. Singh, A. Karchani, and R. S. Myong, "A super-parallel mixed explicit discontinuous Galerkin method for the second-order Boltzmann-based constitutive models of rarefied and microscale gases," Comput. Phys. **157**, 146–163 (2017).
[41]B. Cockburn and C.-W. Shu, "The local discontinuous Galerkin method for time-dependent convection-diffusion systems," SIAM J. Numer. Anal. **35**, 2440 (1998).
[42]B. Cockburn and C.-W. Shu, "The Runge-Kutta discontinuous Galerkin method for conservation laws V: Multidimensional systems," J. Comput. Phys. **141**, 199 (1998).
[43]S. Singh, A. Karchani, and R. S. Myong, "Non-equilibrium effects of diatomic and polyatomic gases on the shock-vortex interaction based on the second-order constitutive model of the Boltzmann-Curtiss equation," Phys. Fluids **30**, 016109 (2018).
[44]S. Singh and R. S. Myong, "A computational study of bulk viscosity effects on shock-vortex interaction using discontinuous Galerkin method," J. Comput. Fluids Eng. **22**, 86–95 (2017).
[45]S. Singh and M. Battiato, "Strongly out-of-equilibrium simulations for electron Boltzmann transport equation using explicit modal discontinuous Galerkin method," Int. J. Appl. Comput. Math. **6**, 1–17 (2020).
[46]S. Singh and M. Battiato, "Effect of strong electric fields on material responses: The Bloch oscillation resonance in high field conductivities," Materials **13**, 1070 (2020).
[47]S. Singh, "Development of a 3D discontinuous Galerkin method for the second-order Boltzmann-Curtiss based hydrodynamic models of diatomic and polyatomic gases," Ph.D. thesis, Gyeongsang National University, South Korea, 2018.
[48]G. Bird, *Molecular Gas Dynamics and the Direct Simulation of Gas Flows* (Clarendon, Oxford, 1994).
[49]A. Marquina and P. Mulet, "A flux-split algorithm applied to conservative models for multicomponent compressible flows," J. Comput. Phys. **185**, 120–138 (2003).
[50]S. Singh, A. Karchani, K. Sharma, and R. S. Myong, "Topology of the second-order constitutive model based on the Boltzmann-Curtiss kinetic equation for diatomic and polyatomic gases," Phys. Fluids **32**, 026104 (2020).

Published under license by AIP Publishing